Robust Deadbeat Predictive Current Control of Permanent Magnet Linear Synchronous Machines Based on Time-Varying Asymmetric Model

Ziyu Zou, *Graduate Student Member, IEEE*, Mengfei Zheng, Yanxin Li, *Member, IEEE*, and Qinfen Lu, *Senior Member, IEEE*

***Abstract*—In permanent magnet linear synchronous machines, the longitudinal end effect gives rise to the manifestation of asymmetric and time-varying characteristics. When employing the model-based deadbeat predictive current control (DPCC), these characteristics can lead to additional disturbances and more intricate stability analysis. To enhance control performance, this article proposes a robust DPCC tailored for time-varying asymmetric machine model. Initially, an analysis is conducted on the disturbances, focusing on those induced by parameter mismatches and their associated frequency characteristics. In order to observe and compensate for various disturbances in time-varying model, the uncertainty and disturbance estimator (UDE) is employed to design one-step prediction and deadbeat control law. Building upon this, the parameter mismatch observer is developed to suppress high-frequency tracking errors while addressing the bandwidth limitations of the UDE. The proposed method not only facilitates a rigorous and concise stability proof for time-varying asymmetric system, but also mitigates disturbances across the entire frequency spectrum. The experimental results validate the effectiveness and superiority of the proposed method.**

***Index Terms*—Deadbeat predictive current control (DPCC), parameter asymmetry, permanent magnet linear synchronous machine (PMLSM), robust control.**

I. Introduction

PERMANENT magnet linear synchronous machines (PMLSMs) are widely employed in precision control applications due to their characteristics of direct drive and high accuracy [1], [2]. To meet the higher demands on current control performance in these scenarios, the deadbeat predictive current control (DPCC) is extensively adopted for its rapid dynamic response and low current ripple [3]. However, the performance of DPCC is highly dependent on machine model and exhibits significant sensitivity to disturbances within the model [4].

To enhance the robustness of DPCC against disturbances, numerous approaches have been proposed for permanent magnet synchronous machines (PMSMs), which can be categorized as follows. First, some studies construct compensation terms based on the error between the measured and the predicted currents to correct the voltage commands [5]. In view of the sensitivity of DPCC control performance to parameter variations, some researches have incorporated online parameter identification methods to improve robustness [6], [7]. While this approach mitigates the impact of parameter mismatches, their ability to suppress unmodeled disturbances remains limited. The disturbance observer can effectively address various disturbances [8], which has led to extensive research on the combination of disturbance observer and DPCC. In these studies, lumped disturbances are estimated by various observers, including Luenberger observer [9], sliding-mode observer [10], and extended state observer (ESO) [11].

Although the robust DPCC for PMSMs is well-developed, the more complex nature of PMLSM poses additional challenges for enhancing robustness. The differences of PMLSMs arise from the longitudinal end effect, which inevitably leads to the detent force and parameter asymmetry [12]. In particular, the parameter asymmetry affects the electromagnetic performance, highlighting the necessity of addressing asymmetry in control strategies [13], [14]. In DPCC, asymmetry introduces time-varying characteristics [15], which indicates that both the lumped disturbances and the machine model exhibit inherent time-varying behavior.

The time-varying disturbances in DPCC have been analyzed in many existing studies. These disturbances lead to time-varying errors in the current tracking results, which are manifested as current harmonics. In [16], the harmonic reference correcting current is injected to eliminate the harmonics without affecting dynamic performance. Based on the sampled harmonic currents, the control voltages can be calculated to mitigate the harmonics [17]. Since time-varying disturbances are typically characterized by distinct frequency components, DPCC can be

Received 8 February 2025; revised 21 April 2025 and 9 June 2025; accepted 1 July 2025. Date of publication 7 July 2025; date of current version 27 August 2025. This work was supported in part by the National Science Foundation of China under Grant NSFC52177061 and Grant NSFC52107061 and in part by the Natural Science Foundation of Zhejiang Province under Grant LZ23E070002. Recommended for publication by Associate Editor X. Pei. *(Corresponding authors: Yanxin Li; Qinfen Lu.)*

The authors are with the College of Electrical Engineering, Zhejiang University, Zhejiang 310027, China (e-mail: eezouziyu@zju.edu.cn; m.z@zju.edu.cn; eeliyanxin@zju.edu.cn; luqinfen@zju.edu.cn).

Color versions of one or more figures in this article are available at https://doi.org/10.1109/TPEL.2025.3586611.

Digital Object Identifier 10.1109/TPEL.2025.3586611

integrated with a resonant controller to effectively suppress them [18]. In addition, the extended model of disturbances can be established, then the disturbances along with their derivatives can be estimated based on the Kalman filter [19], thereby facilitating the compensation of time-varying disturbances.

The aforementioned methods are aimed to address time-varying disturbances of PMSMs. However, as previously mentioned, the asymmetric model of PMLSMs is inherently time-varying, which transforms the entire control system into the linear time-varying (LTV) system. The stability analysis of LTV systems is significantly more complex than that of linear time-invariant (LTI) systems. Moreover, commonly utilized methods, such as the Routh–Hurwitz stability criterion, cannot be extended to LTV systems [20]. To achieve tracking and suppression of time-varying disturbances within the framework of LTV system, the uncertainty and disturbance estimator (UDE) is adopted in this article. As a robust control strategy, UDE demonstrates broad applicability to both LTI and LTV systems [21]. Compared to conventional disturbance observers, it employs filtering for lumped disturbance estimation and compensation, offering clearer frequency-domain insights into disturbance rejection. Moreover, it possesses excellent disturbance suppression capabilities and has been applied in scenarios such as PMSMs [22] and grid-tied inverters [23]. In this article, the UDE is applied within the control framework of the asymmetric DPCC, which improves disturbance rejection capability without compromising dynamic performance.

When the UDE is embedded into DPCC, its limited bandwidth may fail to meet the demands for suppressing high-frequency (HF) disturbances caused by excessive inductance parameters in DPCC. Although these HF disturbances are difficult to observe directly, they can be effectively suppressed by self-tuning or correction of inductance parameters [24], [25]. In addition, some methods extend conventional disturbance observers by incorporating dedicated inductance observers to compensate for inductance mismatches [26]. Nevertheless, due to the presence of asymmetry in PMLSMs, the inductance is time-varying and coupled, making it challenging to employ conventional estimation methods. Besides, existing parameter estimation methods that consider asymmetry also lack the capability to estimate time-varying parameters [27], [28]. Therefore, the time-varying parameter identification algorithm proposed in [29] is employed to develop the parameter mismatch observer (PMO), thereby suppressing HF disturbances. Compared with existing parameter observer methods, the proposed PMO exhibits superior accuracy and stability in handling the time-varying and coupled inductance within the asymmetric model. Furthermore, the extension and mixing process from [30] is applied to decouple parameter mismatches and simplify the observation.

Based on the time-varying asymmetric model of PMLSM, this article investigates a robust DPCC method. The time-varying lumped disturbances and their frequency characteristics are modeled and analyzed. The UDE is embedded into DPCC to compensate for the lumped disturbances. On this basis, the PMO is employed to eliminate the HF disturbances beyond the bandwidth of UDE. The stability proof and experimental validation for the proposed method are provided. The main contribution of this article can be summarized as follows.

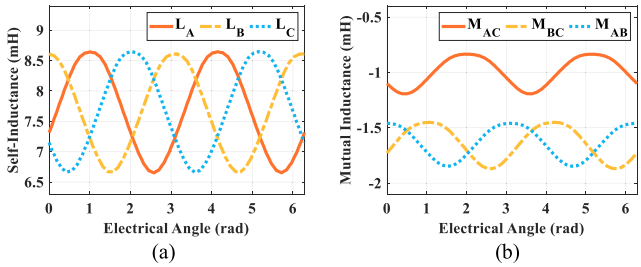

Fig. 1. FE results of inductance. (a) Self-inductance. (b) Mutual inductance.

1) The proposed DPCC is modified based on the asymmetric PMLSM model, leading to a more precise control strategy. In addition, a novel modeling approach and frequency analysis are introduced to characterize the time-varying disturbances in the asymmetric model.
2) The UDE is integrated into the asymmetric DPCC framework to address challenges in the stability analysis of LTV systems. By improving the UDE, the proposed method achieves enhanced disturbance rejection while maintaining good dynamic performance.
3) The PMO is employed to observe the asymmetric inductance mismatch matrix, thereby broadening the disturbance suppression bandwidth. The design of the PMO explicitly accounts for the time-varying and coupling characteristics of the asymmetric model, which enhances its generality and stability in the observation and compensation of parameter mismatches.

The rest of this article is organized as follows. In Section II, the modified DPCC considering asymmetry is proposed. The time-varying disturbances are modeled and analyzed in Section III. The proposed robust DPCC that incorporates UDE and PMO is introduced in Section IV, and the robustness proof for the LTV system is provided. In Section V, the verification experiments of the robustness are conducted. Finally, Section VI concludes this article.

II. Asymmetric Model and Modified DPCC

A. Time-Varying Asymmetric Model of PMLSM

To PMLSMs, the linear structure leads to discontinuity at longitudinal direction, which causes longitudinal end effect. This inevitably causes an asymmetric spatial distribution of the three-phase windings, thereby introducing asymmetry into the inductance parameters, which is influenced by machine topologies. To the studied flat PMLSM prototype, the finite element (FE) simulation results of the self-inductances and mutual inductances are shown in Fig. 1. It can be observed that the ac mutual inductance exhibits noticeable asymmetry.

To achieve higher modeling accuracy for PMLSM, asymmetry is incorporated into the model. According to [28], the asymmetric component is introduced into the three-phase inductance matrix, which is then substituted into the three-phase machine equation. By subsequently transforming the model

into the synchronous reference frame, the asymmetric machine model can be derived as

$$\begin{bmatrix} u_d \\ u_q \end{bmatrix} = \begin{bmatrix} R_s - \gamma\omega_e \sin(2\theta_r + b_r) & -\omega_e L_q - \gamma\omega_e \cos(2\theta_r + b_r) \\ \omega_e L_d - \gamma\omega_e \cos(2\theta_r + b_r) & R_s + \gamma\omega_e \sin(2\theta_r + b_r) \end{bmatrix} \times \begin{bmatrix} i_d \\ i_q \end{bmatrix} + \begin{bmatrix} L_d + \gamma\cos(2\theta_r + b_r) & -\gamma\sin(2\theta_r + b_r) \\ -\gamma\sin(2\theta_r + b_r) & L_q - \gamma\cos(2\theta_r + b_r) \end{bmatrix} \begin{bmatrix} pi_d \\ pi_q \end{bmatrix} + \omega_e \psi_f \begin{bmatrix} 0 \\ 1 \end{bmatrix} \quad (1)$$

where p is the differential operator; u_d, u_q and i_d, i_q are the voltages and currents; ω_e is the machine electrical angular velocity; θ_r is the electrical angle; R_s is the phase resistance; ψ_f is the permanent magnet flux linkage. L_d and L_q represent the dc components of the inductance matrix, γ and b_r denote the magnitude and phase of asymmetric component. Their relationship with the symmetric inductances $L_{\mathrm{d}0}$, $L_{\mathrm{q}0}$ can be found in [28]. The established asymmetric model (1) is capable of describing various asymmetric conditions in PMLSMs. Accordingly, the robust enhancement method developed from this model is applicable to all asymmetric cases, thereby improving its generality and adaptability.

Compared to PMSM, the additional time-varying and nonlinear components are introduced into the PMLSM due to parameter asymmetry, which degrades the control accuracy and stability of the DPCC based on the conventional symmetric model.

B. Modified DPCC Considering Asymmetry

To mitigate the impact of asymmetry on control, the DPCC is modified based on the established time-varying asymmetric model of PMLSM. Utilizing the forward Euler discretization method, the discretized model expression at the kth control cycle can be obtained as

$$\begin{bmatrix} u_d(k) \\ u_q(k) \end{bmatrix} = \boldsymbol{G}(k) \begin{bmatrix} i_d(k) \\ i_q(k) \end{bmatrix} + \boldsymbol{H}(k) \frac{1}{T_s} \begin{bmatrix} i_d(k+1) - i_d(k) \\ i_q(k+1) - i_q(k) \end{bmatrix} + \boldsymbol{\Omega}(k) \quad (2)$$

where

$$\boldsymbol{G}(k) = \begin{bmatrix} R_s - \omega_e(k)\gamma\sin\beta(k) & -\omega_e(k)[L_q + \gamma\cos\beta(k)] \\ \omega_e(k)[L_d - \gamma\cos\beta(k)] & R_s + \omega_e(k)\gamma\sin\beta(k) \end{bmatrix}$$

$$\boldsymbol{H}(k) = \begin{bmatrix} L_d + \gamma\cos\beta(k) & -\gamma\sin\beta(k) \\ -\gamma\sin\beta(k) & L_q - \gamma\cos\beta(k) \end{bmatrix},$$

$$\boldsymbol{\Omega}(k) = \begin{bmatrix} 0 \\ \omega_e(k)\psi_f \end{bmatrix}, \ \beta(k) = 2\theta_r(k) + b_r, \ T_\mathrm{s} \text{ denotes the control period.}$$

In digital control systems, the execution time needed for sampling and control algorithm causes the delay of one control period in the output voltage. To prevent instability due to this delay, the compensation is incorporated into DPCC, which requires the one-step prediction as

$$\begin{bmatrix} i_d^p(k+1) \\ i_q^p(k+1) \end{bmatrix} = \boldsymbol{P}(k) \begin{bmatrix} i_d(k) \\ i_q(k) \end{bmatrix} + \boldsymbol{Q}(k) \begin{bmatrix} u_d(k) \\ u_q(k) \end{bmatrix} - \boldsymbol{Q}(k)\boldsymbol{\Omega}(k) \quad (3)$$

where $\boldsymbol{P}(k) = \boldsymbol{I} - T_s\boldsymbol{H}^{-1}(k)\boldsymbol{G}(k)$, $\boldsymbol{Q}(k) = T_s\boldsymbol{H}^{-1}(k)$, $i_\mathrm{d}{}^\mathrm{p}$ and $i_\mathrm{q}{}^\mathrm{p}$ are the predicted currents, and $\boldsymbol{I}$ is the identify matrix.

Since the mechanical time constant is much larger than the electrical time constant, the speed and electrical angle can be considered constant within adjacent control cycles. Thus, it is obtained that $\omega_\mathrm{e}(k{+}1) = \omega_\mathrm{e}(k)$, $\boldsymbol{G}(k{+}1) = \boldsymbol{G}(k)$, $\boldsymbol{H}(k{+}1) = \boldsymbol{H}(k)$. Subsequently, based on the deadbeat control law, the reference voltage for the (k+1)th control cycle can be calculated as

$$\begin{bmatrix} u_d^*(k+1) \\ u_q^*(k+1) \end{bmatrix} = \boldsymbol{G}(k) \begin{bmatrix} i_d^p(k+1) \\ i_q^p(k+1) \end{bmatrix} + \boldsymbol{H}(k) \frac{1}{T_s} \begin{bmatrix} i_d^* - i_d^p(k+1) \\ i_q^* - i_q^p(k+1) \end{bmatrix} + \boldsymbol{\Omega}(k) \quad (4)$$

where $u_\mathrm{d}{}^*$, $u_\mathrm{q}{}^*$and $i_\mathrm{d}{}^*$, $i_\mathrm{q}{}^*$ are the reference voltages and currents.

Due to the time-varying asymmetric model, the control system based on the modified DPCC has been transformed into a LTV system. Moreover, the modified DPCC exhibits significant nonlinearity and coupling effects, rendering conventional disturbance and stability analysis unsuitable.

III. Disturbance Modeling and Analysis

In practical applications, disturbances inevitably arise in machine model. Besides, the disturbances in asymmetric PMLSMs differ from those in PMSMs. Accordingly, the PMLSM model incorporating disturbances is established as

$$\begin{bmatrix} u_d \\ u_q \end{bmatrix} = \begin{bmatrix} \hat{R}_s - \omega_e\hat{\gamma}\sin\hat{\beta} & -\omega_e\left(\hat{L}_q + \hat{\gamma}\cos\hat{\beta}\right) \\ \omega_e\left(\hat{L}_d - \hat{\gamma}\cos\hat{\beta}\right) & \hat{R}_s + \omega_e\hat{\gamma}\sin\hat{\beta} \end{bmatrix} \begin{bmatrix} i_d \\ i_q \end{bmatrix} + \begin{bmatrix} \hat{L}_d + \hat{\gamma}\cos\hat{\beta} & -\hat{\gamma}\sin\hat{\beta} \\ -\hat{\gamma}\sin\hat{\beta} & \hat{L}_q - \hat{\gamma}\cos\hat{\beta} \end{bmatrix} p \begin{bmatrix} i_d \\ i_q \end{bmatrix} + \begin{bmatrix} 0 \\ \omega_e\hat{\psi}_f \end{bmatrix} + \begin{bmatrix} f_d \\ f_q \end{bmatrix} \quad (5)$$

where $\hat{\mathrm{x}}$ represents the nominal value of the parameters ($x = R_\mathrm{s}$, ψ_f, L_d, L_q, γ, β), f_d and f_q denote the lumped disturbances, whose specific expressions are

$$\begin{cases} f_d = \Delta R i_d - \Delta L_q\omega_e i_q + \Delta L_d p i_d \\ \qquad -\Delta S\omega_e i_d - \Delta C\omega_e i_q + \Delta C p i_d - \Delta S p i_q + \varepsilon_d \\ f_q = \Delta R i_q + \Delta L_d\omega_e i_d + \Delta L_q p i_q + \Delta\psi_f\omega_e \\ \qquad -\Delta C\omega_e i_d + \Delta S\omega_e i_q - \Delta S p i_d - \Delta C p i_q + \varepsilon_q \end{cases} \quad (6)$$

where $\Delta\mathrm{x}$ denotes the mismatch between the real value and the nominal value of the parameters, i.e., $x = \hat{\mathrm{x}} + \Delta\mathrm{x}$ ($x = R_\mathrm{s}$, ψ_f, L_d, L_q). ε_d and ε_q are disturbances caused by factors other than the model parameters, which will be discussed in detail later. ΔS

and ΔC are the components related to the asymmetric parameter mismatch, as shown in

$$\begin{cases} \Delta S = (\hat{\gamma} + \Delta\gamma)\sin\left(2\theta_r + \hat{b}_r + \Delta b_r\right) - \hat{\gamma}\sin\left(2\theta_r + \hat{b}_r\right) \\ \Delta C = (\hat{\gamma} + \Delta\gamma)\cos\left(2\theta_r + \hat{b}_r + \Delta b_r\right) - \hat{\gamma}\cos\left(2\theta_r + \hat{b}_r\right). \end{cases} \tag{7}$$

It is observed that ΔS and ΔC introduced by asymmetry lead to time-varying disturbances. Besides, the disturbances caused by mismatches in other parameters undergo modifications due to asymmetry. Therefore, the following analysis focuses on the various disturbances in the asymmetric model.

A. Disturbance of Inductance Mismatch

According to (6), the current frequency characteristics can be introduced into the lumped disturbances. Therefore, the current tracking performance under inductance mismatch are analyzed. By considering the one-step delay, the derivation yields a more accurate error model. Based on the prediction (3), the real current and the predicted current at (k+1)th control cycle can be obtained as

$$\begin{cases} \boldsymbol{I}_s^r\ (k+1) = \boldsymbol{P}\,(k)\,\boldsymbol{I}_s^r\,(k) + \boldsymbol{Q}\,(k)\,[\boldsymbol{U}\,(k) - \boldsymbol{\Omega}\,(\mathrm{k})] \\ \boldsymbol{I}_s^p\ (k+1) = \hat{\boldsymbol{P}}\ (k)\,\boldsymbol{I}_s^r\,(k) + \hat{\boldsymbol{Q}}\,(k)\left[\boldsymbol{U}\,(k) - \hat{\boldsymbol{\Omega}}\,(\mathrm{k})\right] \end{cases} \tag{8}$$

where $\boldsymbol{I}_s{}^{\mathrm{r}}$ and $\boldsymbol{I}_s{}^{\mathrm{p}}$ are the real and the predicted current vectors, $\boldsymbol{X}$ and $\hat{\boldsymbol{X}}$ represent the real and nominal parameter matrices ($\boldsymbol{X} = \boldsymbol{P}$, $\boldsymbol{Q}$, Ω). Based on (4), the reference voltage can be calculated. By substituting the reference voltage into the prediction step, the real current at (k+2)th control cycle can be obtained. Due to the small value of T_{s}, it is assumed that $R_{\mathrm{s}}T_{\mathrm{s}}/L_{\mathrm{dq}} \ll 1$ and $\omega_{\mathrm{e}}T_{\mathrm{s}} \ll 1$. Subsequently, the current relationship is derived as

$$\begin{aligned} \boldsymbol{I}_s^*\ (k+2) = {} & \hat{\boldsymbol{H}}^{-1}\ (k)\,\boldsymbol{H}\,(k)\,\boldsymbol{I}_s^r\,(k+2) \\ & - \hat{\boldsymbol{H}}^{-1}\,(k)\left[\boldsymbol{H}\,(k) - \hat{\boldsymbol{H}}\,(k)\right]\boldsymbol{I}_s^r\,(k). \end{aligned} \tag{9}$$

By recursively applying the above equation, the expressions for the real current can be further derived. When $n = 2N$+1, $N \in \mathbb{N}*$, the real current can be formulated as (10), where $m = 2i$-1

$$\begin{aligned} \boldsymbol{I}_s^r\ (n) = {} & \boldsymbol{H}^{-1}\ (n)\,\hat{\boldsymbol{H}}\,(n)\,\boldsymbol{I}_s^*\,(n) \\ & + \sum_{k=1,3,\ldots,n-2}\left\{\prod_{i=\frac{k+3}{2}}^{\frac{n+1}{2}}\left[\boldsymbol{I} - \boldsymbol{H}^{-1}\,(m)\,\hat{\boldsymbol{H}}\,(m)\right]\right\} \\ & \times \boldsymbol{H}^{-1}\,(k)\,\hat{\boldsymbol{H}}\,(k)\,\boldsymbol{I}_s^*\,(k) \end{aligned} \tag{10}$$

when $n = 2N$+2, $N \in \mathbb{N}*$, the real current is expressed as

$$\begin{aligned} \boldsymbol{I}_s^r\ (\boldsymbol{n}) = {} & \boldsymbol{H}^{-1}\ (n)\,\hat{\boldsymbol{H}}\,(n)\,\boldsymbol{I}_s^*\,(n) \\ & + \sum_{k=2,4,\ldots,n-2}\left\{\prod_{i=\frac{k+2}{2}}^{\frac{n}{2}}\left[I - \boldsymbol{H}^{-1}\,(2i)\,\hat{\boldsymbol{H}}\,(2i)\right]\right\} \\ & \times \boldsymbol{H}^{-1}\,(k)\,\hat{\boldsymbol{H}}\,(k)\,\boldsymbol{I}_s^*\,(k). \end{aligned} \tag{11}$$

The following illustration will be based on the equations for $n = 2N$+1, and the reference current is set to a constant value to facilitate the analysis. As previously mentioned, the parameter matrices within adjacent control cycles can be considered constant. By premultiplying the real current with $(\boldsymbol{I} - \boldsymbol{H}^{-1}\hat{\boldsymbol{H}})$ and subtracting the resulting expression from the original equation, the current tracking errors can be further derived, which can be expressed as (12), where $\boldsymbol{\Delta I}_s^r = \boldsymbol{I}_s^* - \boldsymbol{I}_s^{\mathrm{r}}$

$$\begin{aligned} \boldsymbol{\Delta I}_s^r\ (\boldsymbol{n}) = {} & \left[\hat{\boldsymbol{H}}^{-1}\,(n)\,\boldsymbol{H}\,(n) - \boldsymbol{I}\right] \\ & \times \left\{\prod_{i=2}^{\frac{n+1}{2}}\left[\boldsymbol{I} - \boldsymbol{H}^{-1}\,(2i-1)\,\hat{\boldsymbol{H}}\,(2i-1)\right]\right\} \\ & \times \boldsymbol{H}^{-1}\,(1)\,\hat{\boldsymbol{H}}\,(1)\,\boldsymbol{I}_s^*\,. \end{aligned} \tag{12}$$

In (12), the tracking errors are composed of the product of parameter matrices. Through diagonalization, its fundamental terms $\boldsymbol{R}$ is decomposed as

$$\boldsymbol{R}\,(k) = \boldsymbol{I} - \boldsymbol{H}^{-1}\,(k)\,\hat{\boldsymbol{H}}\ (k) = \boldsymbol{M}\,(k)\,\boldsymbol{\Lambda}\,(k)\,\boldsymbol{M}^{-1}\,(k) \tag{13}$$

where $\boldsymbol{M}$ is the modal matrix for $\boldsymbol{R}$, Λ is the spectral matrix, which is a diagonal matrix with the eigenvalues λ_1 and λ_2 of $\boldsymbol{R}$ as its diagonal entries.

The product term in (12) can be further derived as follows:

$$\begin{aligned} & \prod_{i=2}^{\frac{n+1}{2}}\left[\boldsymbol{I} - \boldsymbol{H}^{-1}\,(2i-1)\,\hat{\boldsymbol{H}}\,(2i-1)\right] \\ & \quad = \boldsymbol{M}\,(n)\left\{\prod_{i=2}^{\frac{n+1}{2}}\boldsymbol{\Lambda}\,(2i-1)\right\}\boldsymbol{M}^{-1}\,(3). \end{aligned} \tag{14}$$

Based on (12) and (14), the relationship between the tracking errors in adjacent control cycles can be derived as

$$\begin{aligned} \boldsymbol{\Delta I}_s^r\ (n+2) = {} & \begin{bmatrix} \lambda_1\,(n+2) & 0 \\ 0 & \lambda_2\,(n+2) \end{bmatrix} \\ & \times \left[\hat{\boldsymbol{H}}^{-1}\,(n+2)\,\boldsymbol{H}\,(n+2) - \boldsymbol{I}\right]\boldsymbol{M}\,(n+2) \\ & \times \boldsymbol{M}^{-1}\,(n)\left[\hat{\boldsymbol{H}}^{-1}\,(n)\,\boldsymbol{H}\,(n) - \boldsymbol{I}\right]^{-1}\boldsymbol{\Delta I}_s^r\,(n). \end{aligned} \tag{15}$$

According to (15), the frequency characteristics of the tracking errors are primarily determined by the eigenvalues λ_1 and λ_2. When L_{d} and L_{q} are mismatched, the matrix $\boldsymbol{R}$ and its eigenvalue relationship can be expressed as

$$\begin{aligned} \boldsymbol{R}\,(k) = {} & \begin{bmatrix} L_d + \gamma\cos\beta\,(k) & -\gamma\sin\beta\,(k) \\ -\gamma\sin\beta\,(k) & L_q - \gamma\cos\beta\,(k) \end{bmatrix}^{-1} \\ & \times \begin{bmatrix} L_d - \hat{L}_d & 0 \\ 0 & L_q - \hat{L}_q \end{bmatrix} \end{aligned} \tag{16}$$

$$\begin{aligned} & \lambda_1\,(k) + \lambda_2\,(k) \\ & \quad = \frac{\Delta L_d\,[L_q - \gamma\cos\beta\,(k)] + \Delta L_q\,[L_d + \gamma\cos\beta\,(k)]}{L_d L_q - (L_d - L_q)\,\gamma\cos\beta\,(k) - \gamma^2} \end{aligned} \tag{17}$$

$$\lambda_1(k)\lambda_2(k) = \frac{\Delta L_d \Delta L_q}{L_d L_q - (L_d - L_q)\gamma\cos\beta(k) - \gamma^2}. \quad (18)$$

When the applied inductance is larger than the real value, all the eigenvalues are negative according to (17) and (18). Given that the parameter matrix can be considered constant over several adjacent control cycles, the tracking errors in (15) exhibit rapid sign changes, with a switching period of four control cycles. Consequently, the tracking errors contain HF components with frequencies reaching up to one quarter of the sampling frequency. It is important to note that this represents only an estimated frequency of the disturbance induced by the excessive inductance. The real frequency characteristics may be more complex due to factors such as the time-varying nature of the asymmetric model. However, the preceding analysis indicates that the frequency of this disturbance is indeed significantly higher than that of conventional harmonic disturbances. When the applied inductance is smaller than the real value, all the eigenvalues are positive, preventing the rapid sign switching phenomenon. In this case, the errors manifest in the low-frequency domain. For asymmetric parameters, the effects of mismatch follow the same principle.

B. Disturbance of Resistance and Flux Linkage Mismatch

Following the same procedure, the expressions for the tracking errors due to resistance and flux linkage mismatches can be formulated as

$$\Delta \boldsymbol{I}_s^r(n) = \frac{2T_s\left(R_s - \hat{R}_s\right)}{L_d L_q - (L_d - L_q)\gamma\cos\beta(k) - \gamma^2} \times \begin{bmatrix} L_q - \gamma\cos\beta(k) & \gamma\sin\beta(k) \\ \gamma\sin\beta(k) & L_d + \gamma\cos\beta(k) \end{bmatrix} \boldsymbol{I}_s^* \quad (19)$$

$$\Delta \boldsymbol{I}_s^r(n) = \frac{\left(\psi_f - \hat{\psi}_f\right) 2\omega_e T_s}{L_d L_q - (L_d - L_q)\gamma\cos\beta(k) - \gamma^2} \times \begin{bmatrix} \gamma\sin\beta(k) \\ L_d + \gamma\cos\beta(k) \end{bmatrix}. \quad (20)$$

It is observed that the errors encompass both dc and second harmonic components in the case of resistance and flux linkage mismatches. Moreover, the errors introduced by asymmetry are incorporated into the lumped disturbances, leading to time-varying components.

C. Unmodeled Disturbances

In addition to the above disturbances, there are also unmodeled disturbances that are independent of models. Among them, the disturbances affecting the current loop include dead-time effects and measurement error effects [8]. They manifest as low-order harmonic voltage and current offsets, which introduce slow time-varying disturbances.

From the abovementioned analysis, it can be concluded that the lumped disturbances not only include dc and low-order harmonic components, but also may introduce HF components in the case of excessive inductance parameters. In the subsequent analysis of disturbance rejection and robust enhancement, the derivation and design will be based on the established asymmetric model (5), which explicitly accounts for lumped disturbances.

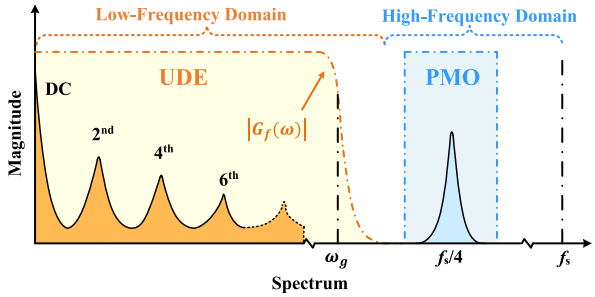

Fig. 2. Illustration of disturbance suppression for the proposed method.

IV. Proposed Robust DPCC Method

To effectively eliminate various disturbances, a robust DPCC method for asymmetric time-varying model is proposed. The UDE method suitable for LTV system is utilized to suppress the time-varying lumped disturbances. Due to the bandwidth limitation of the UDE, it is only capable of effectively observing and suppressing the low-frequency components of the lumped disturbances. To broaden the disturbance rejection range of the proposed method, the PMO is employed to observe and compensate for the time-varying inductance mismatch, thereby eliminating the HF disturbances caused by excessive inductance. The distribution of disturbances corresponding to the two methods is shown in Fig. 2. It should be noted that Fig. 2 serves merely as an intuitive illustration of the frequency-domain distribution of the disturbances addressed by the two methods, whereas the real frequency characteristics of the disturbances are more complex. Nevertheless, since neither method relies on the specific frequency of the disturbances, this does not affect their derivation or design.

A. UDE Implementation Method

In order to enhance robustness, the UDE method is embedded within the asymmetric DPCC framework. This method is based on the time-varying asymmetric model incorporating disturbances, which is further reformulated into the state-space equation as

$$\dot{\boldsymbol{x}} = \boldsymbol{A}(t)\boldsymbol{x} + \boldsymbol{B}(t)\boldsymbol{u} + \boldsymbol{F}(t) \quad (21)$$

where

$$\boldsymbol{x} = \begin{bmatrix} i_d \\ i_q \end{bmatrix}, \boldsymbol{u} = \begin{bmatrix} u_d \\ u_q - \omega_e \psi_f \end{bmatrix} \quad \boldsymbol{F}(t) = -\boldsymbol{B}(t) \begin{bmatrix} f_d(t) \\ f_q(t) \end{bmatrix}$$

$$\boldsymbol{A}(t) = -\hat{\boldsymbol{H}}^{-1}(t)\hat{\boldsymbol{G}}(t), \quad \boldsymbol{B}(t) = \hat{\boldsymbol{H}}^{-1}(t).$$

In (21), the expression for the disturbance can be obtained from the voltage and current. However, due to the presence of current derivate, it is not possible to directly calculate the disturbance at the current control cycle. Therefore, following the principles of the UDE method, an appropriate filter $G_f(s)$ is employed to approximate $\boldsymbol{F}$ as

$$\boldsymbol{F_e}(t) = \boldsymbol{F}(t) \star g_f(t) \quad (22)$$

where $\boldsymbol{F_e}$ is the approximated disturbance, g_f is the impulse response of the filter, "$\star$" denotes the convolution operator.

To facilitate the derivation process for the LTV system, the LTI reference model is introduced as

$$\dot{\boldsymbol{x}}_{\boldsymbol{m}}(t) = \boldsymbol{A_m}\,\boldsymbol{x_m}(t) + \boldsymbol{B_m}\boldsymbol{c}(t) \tag{23}$$

where $\boldsymbol{x_m} = [i_{\mathrm{dm}}, i_{\mathrm{qm}}]^T$ is the reference state vector, $\boldsymbol{c} = [i_{\mathrm{d}}{}^*, i_{\mathrm{q}}{}^*]^T$ denotes the reference current trajectory. $\boldsymbol{A_m}$ and $\boldsymbol{B_m}$ are the coefficient matrices associated with the system bandwidth.

Combining (21) and (23), the error $\boldsymbol{e} = \boldsymbol{x_m} - \boldsymbol{x}$ is obtained as

$$\dot{\boldsymbol{e}} = \boldsymbol{A_m}\,\boldsymbol{e} + [\boldsymbol{A_m}\boldsymbol{x} + \boldsymbol{B_m}\boldsymbol{c} - \boldsymbol{A}(t)\,\boldsymbol{x} - \boldsymbol{B}(t)\,\boldsymbol{u} - \boldsymbol{F}(t)]. \tag{24}$$

The objective of the UDE strategy is to ensure that the system state vector asymptotically tracks the reference state vector in the presence of disturbances. To this end, the filtering approach (22) is employed to estimate the lumped disturbance, thereby deriving the UDE-based control law as

$$\begin{aligned}\boldsymbol{u} = \boldsymbol{B}^{-1}(t)\,[\boldsymbol{A_m}\boldsymbol{x} + \boldsymbol{B_m}\boldsymbol{c} - \boldsymbol{A}(t)\,\boldsymbol{x} \\ - (\dot{\boldsymbol{x}} - \boldsymbol{A}(t)\,\boldsymbol{x} - \boldsymbol{B}(t)\,\boldsymbol{u}) \star g_f].\end{aligned} \tag{25}$$

By substituting the proposed control law and reference model into (21) and applying the Laplace transform, the system state vector in the s-domain can be obtained as

$$\begin{aligned}\boldsymbol{X}(s) = (s\boldsymbol{I} - \boldsymbol{A_m})^{-1}\,\boldsymbol{B_m}\boldsymbol{C}(s) + (s\boldsymbol{I} \\ - \boldsymbol{A_m})^{-1}\,[1 - G_f(s)]\,\boldsymbol{F_s}(s)\end{aligned} \tag{26}$$

where $\boldsymbol{X}(s)$, $\boldsymbol{C}(s)$, and $\boldsymbol{F_s}(s)$ are the Laplace transforms of $\boldsymbol{x}(t)$, $\boldsymbol{c}(t)$, and $\boldsymbol{F}(t)$. According to (26), the UDE method can eliminate the disturbances within the bandwidth of G_{f}. If G_{f} has the unity gain across the entire frequency range of the disturbances, the current can track the reference trajectory without being affected by disturbances. Since the Butterworth filter is simple to implement and has a flat frequency response, it is selected as G_{f}, whose transfer function given as

$$G_f(s) = \frac{\omega_g}{s + \omega_g} \tag{27}$$

where ω_{g} is the disturbance rejection bandwidth of the UDE.

Based on (25), most existing studies directly extract the control input $\boldsymbol{u}$ in the s-domain to formulate the UDE control law [22]. However, this inevitably introduces integral-like operations, which impact the dynamic performance of DPCC. Therefore, the delay operators are adopted to obtain a novel UDE control law that avoids integral operations, which is shown as

$$\begin{aligned}\boldsymbol{u}(t) = \boldsymbol{B}^{-1}(t)\,\{\boldsymbol{A_m}\boldsymbol{x}(t) + \boldsymbol{B_m}\boldsymbol{c}(t) - \boldsymbol{A}(t)\,\boldsymbol{x}(t) \\ - \mathcal{L}^{-1}[sG_f(s)] \star \boldsymbol{x}(t)\} + \boldsymbol{B}^{-1}(t)\,\{\mathcal{L}^{-1}[G_f(s)] \\ \star [\boldsymbol{A}(t_1)\,\boldsymbol{x}(t_1) + \boldsymbol{B}(t_1)\,\boldsymbol{u}(t_1)]\}\end{aligned} \tag{28}$$

where $t_1 = t - T_{\mathrm{s}}$, $\mathcal{L}^{-1}\{\cdot\}$ is the inverse Laplace transform operator. Since the delay operator primarily affects HF components, which lie outside the bandwidth of G_{f}, its application has a negligible impact.

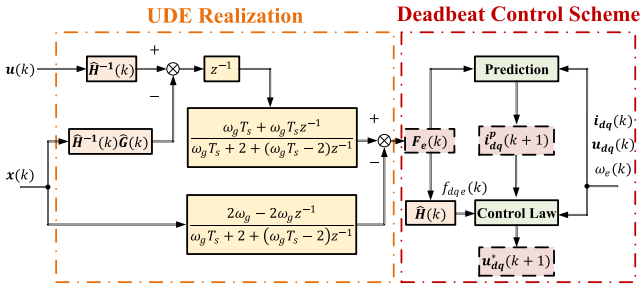

Fig. 3. Diagram of the UDE implementation.

To combine the UDE with the deadbeat control, the coefficient matrices are selected as

$$\boldsymbol{A_m} = \begin{bmatrix} -1/T_s & \\ & -1/T_s \end{bmatrix} \quad \boldsymbol{B_m} = \begin{bmatrix} 1/T_s & \\ & 1/T_s \end{bmatrix}. \tag{29}$$

Substituting into (28) yields the proposed control law as

$$\begin{aligned}\boldsymbol{u}(t) = \hat{\boldsymbol{G}}(t)\,\boldsymbol{x}(t) + \hat{\boldsymbol{H}}(t)\,\frac{1}{T_s}\,[\boldsymbol{c}(t) - \boldsymbol{x}(t)] \\ - \hat{\boldsymbol{H}}(t)\,\mathcal{L}^{-1}[sG_f(s)] \star \boldsymbol{x}(t) + \hat{\boldsymbol{H}}(t)\,\mathcal{L}^{-1}[G_f(s)] \\ \star [\boldsymbol{A}(t_1)\,\boldsymbol{x}(t_1) + \boldsymbol{B}(t_1)\,\boldsymbol{u}(t_1)].\end{aligned} \tag{30}$$

It can be observed that the first two terms of (30) correspond to the conventional control law (4). The remaining term is employed to achieve suppression of the disturbances. This allows for robustness enhancement while maintaining the dynamic performance and tracking bandwidth of the DPCC. In order to eliminate the impact of the one-step delay, the UDE is applied to the prediction and control law. The diagram of the UDE combined with deadbeat control is illustrated in Fig. 3.

B. Time-Varying PMO With Finite-Time Convergence

In practical applications, the bandwidth of G_{f} is limited, and thus, the HF disturbances caused by excessive inductance cannot completely be eliminated by the UDE. Although it is challenging to directly observe and compensate for HF disturbances, the parameter mismatches that give rise to these disturbances are relatively slow-varying. Accordingly, directly observing them can effectively reduce the bandwidth requirements. Therefore, the PMO is proposed to observe the time-varying inductance mismatches within finite time to address HF disturbances.

The proposed PMO extracts and models the HF disturbances based on the predicted current error equation following UDE-based compensation. After applying the UDE, the prediction error is expressed as

$$\dot{\boldsymbol{x}} - \dot{\boldsymbol{x}}_{\boldsymbol{p}} = \boldsymbol{F}(t) \star \mathcal{L}^{-1}[1 - G_f(s)] = \boldsymbol{F_h}(t) \tag{31}$$

where $\dot{\mathrm{x}}_{\mathrm{p}}$ is predicted current derivative, and $\boldsymbol{F_h}$ represents the HF disturbance beyond the bandwidth of UDE. Discretizing the above equation yields

$$\begin{bmatrix} i_d^p(k+1) - i_d(k+1) \\ i_q^p(k+1) - i_q(k+1) \end{bmatrix} = \frac{T_s}{\hat{L}_d\hat{L}_q - \hat{\gamma}(\hat{L}_q - \hat{L}_d)\cos\hat{\beta}(k) - \hat{\gamma}^2}$$

$$\times \begin{bmatrix} \hat{L}_q - \hat{\gamma}\cos\hat{\beta}\,(k) & \hat{\gamma}\sin\hat{\beta}\,(k) \\ \hat{\gamma}\sin\hat{\beta}\,(k) & \hat{L}_d + \hat{\gamma}\cos\hat{\beta}\,(k) \end{bmatrix} \begin{bmatrix} f_{dh}\,(k) \\ f_{qh}\,(k) \end{bmatrix} \tag{32}$$

where f_{dh} and f_{qh} denote the HF components of f_{d} and f_{q}, respectively. They represent the residual disturbances obtained by applying G_{f} to the lumped disturbances formulated in (6). Their specific expressions can be written as

$$\begin{cases} f_{dh} = (\Delta R - \Delta S\omega_e)\ i_{dh} - \omega_e\,(\Delta L_q + \Delta C)\,i_{qh} \\ \qquad + (\Delta L_d + \Delta C)\,pi_{dh} - \Delta S pi_{qh} \\ f_{qh} = \omega_e\ (\Delta L_d - \Delta C)\,i_{dh} + (\Delta R + \Delta S\omega_e)\,i_{qh} \\ \qquad - \Delta S pi_{dh} + (\Delta L_q - \Delta C)\,pi_{qh} \end{cases} \tag{33}$$

where i_{dh}, i_{qh} and pi_{dh}, pi_{qh} denote the HF components of the current and its derivative. To ensure consistency with the disturbance rejection process in (31), the current and its derivative are filtered through G_{f}, and their respective HF components are extracted accordingly. The parameter mismatches in (33) have the same meaning as those defined in (6) and (7). In fact, there will inevitably exist HF unmodeled disturbances in (33). These disturbances are temporarily neglected for the sake of simplicity, and their impact is further analyzed in the stability proof.

The i_{dh} and i_{qh} may contain multiple HF components. The following discussion uses the current i_{h0} with high frequency ω_0 as an example. Performing the Fourier transform on i_{h0} and its derivative to obtain the relationship as

$$I_{h0}\,(\omega) = \mathcal{F}\,[i_{h0}\,(t)] \tag{34}$$

$$pI_{h0}\,(\omega) = \mathcal{F}\ [pi_{h0}\,(t)] = j\omega_0 I_{h0}\,(\omega) \tag{35}$$

where I_{h0} and pI_{h0} are the Fourier transforms of i_{h0} and pi_{h0}, and $\mathcal{F}$ denotes the Fourier transform operator.

To represent the energy and excitation levels of the signals, the two-norms are defined as follows. Based on the Parseval's theorem, they are further transformed into frequency-domain

$$\|i_{h0}\,(t)\|_2 = \sqrt{\textstyle\int_{-\infty}^{+\infty} |i_{h0}\,(t)|^2 dt} = \sqrt{\frac{1}{2\pi}\textstyle\int_{-\infty}^{+\infty} |I_{h0}\,(\omega)|^2 d\omega} \tag{36}$$

$$\begin{aligned} \|pi_{h0}\,(t)\|_2 &= \sqrt{\frac{1}{2\pi}\textstyle\int_{-\infty}^{+\infty} |pI_{h0}\,(\omega)|^2 d\omega} \\ &= \sqrt{\frac{1}{2\pi}\textstyle\int_{-\infty}^{+\infty} \omega_0^2 |I_{h0}\,(\omega)|^2 d\omega}. \end{aligned} \tag{37}$$

Combining (36) and (37), the following relationship can be obtained. And it also applies to other HF components

$$\frac{\|pi_{h0}\,(t)\|_2}{\|i_{h0}\,(t)\|_2} = \omega_0 \gg 1. \tag{38}$$

Therefore, when acting as an excitation, the HF current can be considered negligible in comparison to its derivative. Besides, their corresponding mismatch difference is not significant enough to eliminate the aforementioned gap. On this basis, (32) can be further simplified as

$$\frac{1}{T_{\mathrm{s}}} \begin{bmatrix} \hat{L}_d + \hat{\gamma}\cos\hat{\beta}\,(k) & -\hat{\gamma}\sin\hat{\beta}\,(k) \\ -\hat{\gamma}\sin\hat{\beta}\,(k) & \hat{L}_q - \hat{\gamma}\cos\hat{\beta}\,(k) \end{bmatrix}$$

$$\times \begin{bmatrix} i_{sd}^{p}\,(k+1) - i_{sd}^{r}\,(k+1) \\ i_{sq}^{p}\,(k+1) - i_{sq}^{r}\,(k+1) \end{bmatrix}$$

$$= \begin{bmatrix} \Delta L_d + \Delta C\,(k) & -\Delta S\,(k) \\ -\Delta S\,(k) & \Delta L_q - \Delta C\,(k) \end{bmatrix} \begin{bmatrix} pi_{dh}\,(k) \\ pi_{qh}\,(k) \end{bmatrix}. \tag{39}$$

Based on (39), the mismatched inductance matrix can be observed. In the prediction error equation, the UDE-based compensation has removed the low-frequency disturbances caused by factors such as inverter nonlinearity, the resistance and flux linkage mismatches. Consequently, their adverse influence on the observation of inductance mismatch has been eliminated, thereby enhancing the stability of the compensation. The following illustration takes the d-axis equation as an example. The d-axis linear regression for the mismatch at the kth control cycle can be derived as

$$\begin{aligned} y &= \phi^{\boldsymbol{T}}\ \boldsymbol{\Delta\theta} \\ y &= \frac{1}{T_{\mathrm{s}}} \begin{bmatrix} L_d + \gamma\cos\beta\,(k) & -\gamma\sin\beta\,(k) \end{bmatrix} \begin{bmatrix} i_d^p\,(k) - i_d^r\,(k) \\ i_q^p\,(k) - i_q^r\,(k) \end{bmatrix} \\ \phi^{\boldsymbol{T}} &= \begin{bmatrix} \phi_1 \\ \phi_2 \end{bmatrix}^T = \begin{bmatrix} pi_{dh}\,(k-1) \\ -pi_{qh}\,(k-1) \end{bmatrix}^T, \\ \boldsymbol{\Delta\theta} &= \begin{bmatrix} \Delta\theta_1 \\ \Delta\theta_2 \end{bmatrix} = \begin{bmatrix} \Delta L_d + \Delta C\,(k-1) \\ \Delta S\,(k-1) \end{bmatrix}. \end{aligned} \tag{40}$$

By employing the LTI operators such as delay operators [30], the linear regression equation is extended to obtain

$$\begin{aligned} \boldsymbol{Y_E} &= \phi_{\boldsymbol{E}}\ \boldsymbol{\Delta\theta} \\ \boldsymbol{Y_E} &= \begin{bmatrix} y \\ y_e \end{bmatrix}, \phi_{\boldsymbol{E}} = \begin{bmatrix} \phi_1 & \phi_2 \\ \phi_{1e} & \phi_{2e} \end{bmatrix} \end{aligned} \tag{41}$$

where y_{e}, $\phi_{1\mathrm{e}}$, and $\phi_{2\mathrm{e}}$ represent the outputs of the operators. To simplify the observer design, the adjunct matrix is applied to (41), resulting in the decoupled matrix, as shown in

$$\begin{aligned} \boldsymbol{Y_D} &= \phi_{\boldsymbol{D}}\ \boldsymbol{\Delta\theta} \\ \boldsymbol{Y_D} &= \mathrm{adj}\,(\phi_{\boldsymbol{E}})\,\boldsymbol{Y_E} := \begin{bmatrix} Y_1 & Y_2 \end{bmatrix}^T \\ \phi_{\boldsymbol{D}} &= \mathrm{adj}\,(\phi_{\boldsymbol{E}})\ \phi_{\boldsymbol{E}} = \begin{bmatrix} \rho & \\ & \rho \end{bmatrix},\ \rho = \det\,(\phi_{\boldsymbol{E}})\,. \end{aligned} \tag{42}$$

According to (42), for each mismatch to be observed, there exists a corresponding separate scalar expression as

$$Y_i = \rho\Delta\theta_i, i = 1, 2. \tag{43}$$

Due to the time-varying nature of the parameter mismatches in asymmetric model, conventional observers encounter difficulties in achieving accurate and stable observation. Thus, a nonlinear estimation method is adopted in this article. To prevent reduced observation accuracy due to insufficient excitation after mismatch compensation, the time-varying mismatches need to converge within a finite time, after which observed results are employed for compensation. Therefore, the finite-time convergence estimator is employed as

$$\dot{\Delta\hat{\theta}}_i\ (t) = \gamma_i\,\rho\,(t)\,\lceil Y_i\,(t) - \rho\,(t)\,\Delta\hat{\theta}_i(t)\rfloor^{\alpha} \tag{44}$$

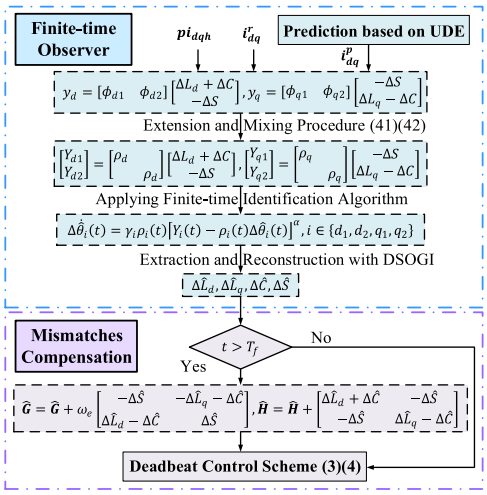

Fig. 4. Flowchart of the proposed PMO method.

where $\Delta\hat{\theta}_{\mathrm{i}}$ is the estimated mismatch, γ_{i} is the convergence coefficient, and $\lceil\cdot\rfloor^{\alpha} := |\cdot|^{\alpha}\mathrm{sign}(\cdot)$, $\alpha\in(0,1)$.

With the designed γ, the time-varying mismatches converge within the finite time T_{f}. Subsequently, utilizing the estimated mismatches for compensation can eliminate HF disturbances.

After compensation, the significant reduction of HF currents results in decreased excitation, making it challenging to update the time-varying mismatches. Therefore, the dual second-order generalized integrator (DSOGI) [28] is employed during the finite-time convergence period. It can extract the amplitude and phase of the time-varying components in mismatches, thereby reconstructing ΔS and ΔC after compensation. Accordingly, the observed HF lumped disturbances can be represented by

$$\begin{cases} \hat{f}_{dh} = \left(\Delta\hat{L}_d + \Delta\hat{C}\right) pi_{dh} - \Delta\hat{S} pi_{qh} \\ \hat{f}_{qh} = -\Delta\hat{S} pi_{dh} + \left(\Delta\hat{L}_q - \Delta\hat{C}\right) pi_{qh}. \end{cases} \tag{45}$$

As demonstrated above, the proposed PMO enables the observation of the entire time-varying inductance mismatch matrix, thereby effectively suppressing the disturbances introduced by time-varying and coupled inductance in observation and control. The flowchart of the PMO method is shown in Fig. 4. It is important to note that the observation relies on HF current excitation, making it applicable only to the observation of excessive inductance. However, since the disturbances caused by inductance being smaller than real value consist of low-frequency components, which can be mitigated by UDE, this limitation does not affect the disturbance rejection capability.

C. Stability Validation

It is necessary to prove the stability of the proposed method for the time-varying asymmetric system within the finite time.

First, the convergence characteristics of the observed time-varying parameter mismatch are analyzed. Due to the introduction of a nonlinear estimator in the PMO, conventional linear control stability analysis methods are not applicable. Therefore, the Lyapunov stability method is employed to analyze the stability and convergence characteristics of the PMO. The linear regression that accounts for disturbances is written as

$$Y(t) = \rho(t)\Delta\theta(t) + \varepsilon(t) \tag{46}$$

where ε represents the residual unmodeled disturbance after UDE filtering, and its upper bound is denoted as ε_{m}. Y and $\Delta\theta$ are the input and the mismatch. The lower bound of the $|\rho|$ is denoted as ρ_{m}. By applying the finite-time estimator (44), the observation error $e(t)$ can be expressed as

$$\dot{e}(t) = -\gamma\rho(t)\lceil\rho(t)e(t) - \varepsilon(t)\rfloor^{\alpha} - \Theta(t) \tag{47}$$

where $e(t) = \Delta\hat{\theta}(t) - \Delta\theta(t)$, $\Theta(t) = \Delta\dot{\theta}(t)$.

Consider the Lyapunov function candidate $V(e) = 0.5e^2$, and its time derivative along the trajectories of the error system is

$$\dot{V}(t) = e(t) \times \left\{-\gamma\rho(t)\lceil\rho(t)e(t) - \varepsilon(t)\rfloor^{\alpha} - \Theta(t)\right\}. \tag{48}$$

With limited mismatch change rate, (48) may be bounded as

$$\dot{V}(t) \le -e(t) \times \gamma\rho(t)\lceil\rho(t)e(t) - \varepsilon(t)\rfloor^{\alpha} + |e(t)|\Theta_m \tag{49}$$

where Θ_{m} is the upper bound of the mismatch change rate. Under the condition that $0<\alpha<1$, the inequality (50) holds [29]

$$-|\rho(t)e(t) - \varepsilon(t)|^{\alpha} \le -|\rho(t)e(t)|^{\alpha} + |\varepsilon(t)|^{\alpha}. \tag{50}$$

Owing to the suppression of the majority of unmodeled disturbances within the UDE, ε satisfies

$$|\rho(t)e(t)| \ge |\varepsilon(t)|. \tag{51}$$

Based on (51), it can be obtained that

$$\mathrm{sign}\left[\rho(t)e(t) - \varepsilon(t)\right] = \mathrm{sign}\left[\rho(t)e(t)\right]. \tag{52}$$

Following that, (49) can be further derived as

$$\dot{V}(t) \le -\gamma|\rho(t)e(t)|^{\alpha+1} + \gamma|\varepsilon(t)|^{\alpha}|\rho(t)e(t)| + |e(t)|\Theta_m. \tag{53}$$

To address the additional terms arising from disturbances and time-varying mismatches, (53) is modified as

$$\begin{aligned} \dot{V}(t) \le & -\gamma(1-\delta)|\rho(t)e(t)|^{\alpha+1} \\ & -\gamma\delta|\rho(t)e(t)|^{\alpha+1} + \left(\Theta_m + \gamma|\varepsilon(t)|^{\alpha}|\rho(t)|\right)|e(t)| \end{aligned} \tag{54}$$

where $\delta\in(0,1)$. When the last two terms of the above inequality are nonpositive, it is obtained that

$$|e(t)| \ge \left(\frac{\Theta_m}{\gamma\delta|\rho(t)|^{\alpha+1}} + \frac{|\varepsilon(t)|^{\alpha}}{\delta|\rho(t)|^{\alpha}}\right)^{\frac{1}{\alpha}}. \tag{55}$$

In this case, (54) can be derived as

$$\dot{V}(t) \le -2^{\frac{\alpha+1}{2}}\gamma(1-\delta)|\rho(t)|^{\alpha+1}V^{\frac{\alpha+1}{2}}(t). \tag{56}$$

Integrating the above inequality yields

$$\begin{aligned} V^{-\frac{\alpha-1}{2}}(t) \le & V^{-\frac{\alpha-1}{2}}(t_0) \\ & -(1-\alpha)\int_{t_0}^{t} 2^{\frac{\alpha-1}{2}}\gamma(1-\delta)|\rho(\tau)|^{\alpha+1}d\tau \end{aligned} \tag{57}$$

where t_0 is the initial time. As illustrated in Section II, the excessive inductance results in HF disturbances, thereby ensuring that

the excitation term ρ satisfies the persistent excitation condition. According to [31], it is expressed as

$$\frac{1}{T}\int_t^{t+T}|\rho(\tau)|\,d\tau \geq \epsilon,\ \forall t \geq t_0 \tag{58}$$

for some T, $\epsilon > 0$, where ϵ represents the lower bound of the excitation. According to the Hölder's inequality, (58) can be further transformed into

$$\int_t^{t+T}|\rho(\tau)|^{\alpha+1}d\tau \geq \frac{1}{T^p}\left(\int_t^{t+T}|\rho(\tau)|\,d\tau\right)^{\alpha+1} \geq T\epsilon^{\alpha+1}. \tag{59}$$

From (57) and (59), it follows that:

$$V^{-\frac{\alpha-1}{2}}(t_0+T) \leq V^{-\frac{\alpha-1}{2}}(t_0)-(1-\alpha)\,2^{\frac{\alpha-1}{2}}\gamma(1-\delta)\,T\epsilon^{\alpha+1}. \tag{60}$$

Based on the above inequality, the boundary point of the convergence time is given by

$$T_0 = \frac{V^{\frac{1-\alpha}{2}}(t_0)}{(1-\alpha)\,2^{\frac{\alpha-1}{2}}\gamma(1-\delta)\,\epsilon^{\alpha+1}} = \frac{|e(t_0)|^{1-\alpha}}{(1-\alpha)(1-\delta)\gamma\epsilon^{\alpha+1}}. \tag{61}$$

When $t \leq T_0$, the dynamic process of the error satisfies

$$e(t) \leq \left[e^{1-\alpha}(t_0) - (1-\alpha)\gamma(1-\delta)(t-t_0)\,\epsilon^{\alpha+1}\right]^{\frac{1}{1-\alpha}}. \tag{62}$$

Furthermore, the error is ultimately bounded as

$$|e(t)| \leq \left(\frac{\Theta_m}{\gamma\delta|\rho_m|^{\alpha+1}} + \frac{|\varepsilon_m|^{\alpha}}{\delta|\rho_m|^{\alpha}}\right)^{\frac{1}{\alpha}},\ \forall t \geq T_0. \tag{63}$$

By ensuring γ satisfy (64), the observation error can converge to the above bound within the finite time T_{f}

$$\gamma \geq \frac{|e(t_0)|^{1-\alpha}}{(1-\alpha)(1-\delta)T_f\epsilon^{\alpha+1}}. \tag{64}$$

Upon completion of the observation, the reconstructed mismatches from DSOGI are incorporated into asymmetric DPCC, which consequently mitigates the HF disturbances induced by excessive inductance. At this point, all remaining disturbances fall within the rejection bandwidth ω_{g} of the UDE method and can be suppressed. Ultimately, the current tracking dynamics with the proposed method in the s-domain can be expressed as

$$\begin{bmatrix} I_d(s) \\ I_q(s) \end{bmatrix} = \begin{bmatrix} \frac{1}{T_s s+1} & \\ & \frac{1}{T_s s+1} \end{bmatrix} \begin{bmatrix} I_d^*(s) \\ I_q^*(s) \end{bmatrix}. \tag{65}$$

From the above derivation, it can be concluded that the proposed method can track the reference current with the same bandwidth as conventional DPCC while suppressing various disturbances within the finite time. Therefore, its good robustness is demonstrated.

V. Experimental Validation

To demonstrate the effectiveness of the proposed method, experimental validation has been conducted. The block diagram of the machine control system incorporating the proposed robust DPCC is shown in Fig. 5. In the proposed method, both the UDE and PMO perform disturbance observation and compensation within the same control cycle, ensuring simultaneous execution.

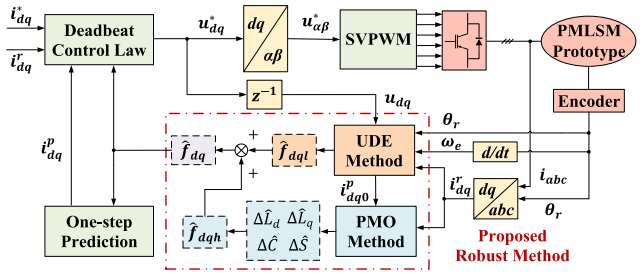

Fig. 5. Block diagram of the proposed robust DPCC system.

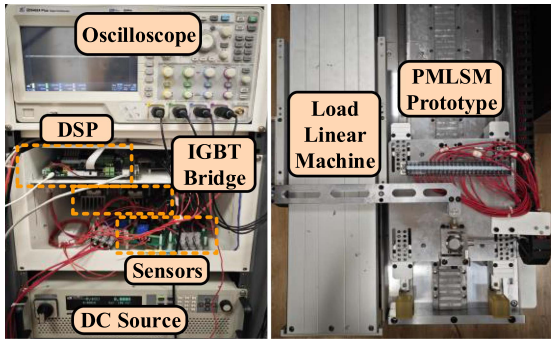

Fig. 6. PMLSM prototype and experiment platform.

TABLE I
Parameters of PMLSM Prototype

Parameters	Value
Stator Resistance (Ω), R_s	0.7
PM Flux Linkage (Wb), ψ_f	0.05
d-axis Symmetric Inductance (mH), L_{d0}	10
q-axis Symmetric Inductance (mH), L_{q0}	11.6
Asymmetric Component (mH), γ	0.97
Asymmetric Phase Parameter (°), b_r	120

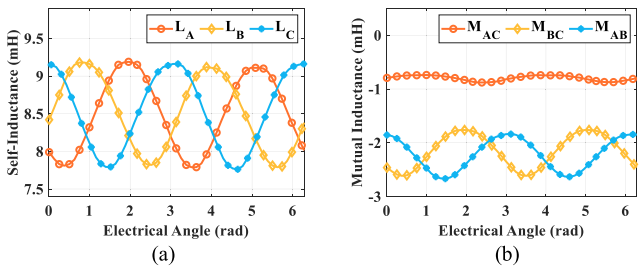

Fig. 7. Measured inductance. (a) Self-inductance. (b) Mutual inductance.

The experiments are carried out on the platform shown in Fig. 6, which consists of the PMLSM prototype, load machine, and the digital control system. The TMS320F28379D DSP is employed as the processor for the controller, with an update frequency of 20 kHz. The experimental data is stored in the oscilloscope and exported for subsequent processing.

The parameters of the PMLSM prototype are listed in Table I in detail. In particular, the measured inductance is depicted in

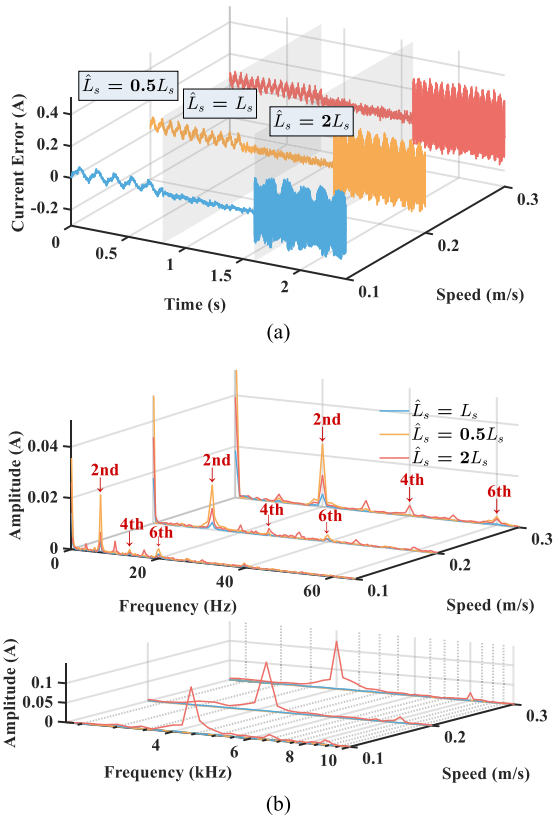

Fig. 8. Current errors and spectrum under inductance mismatches at three operating speeds. (a) Current errors. (b) The Spectrum.

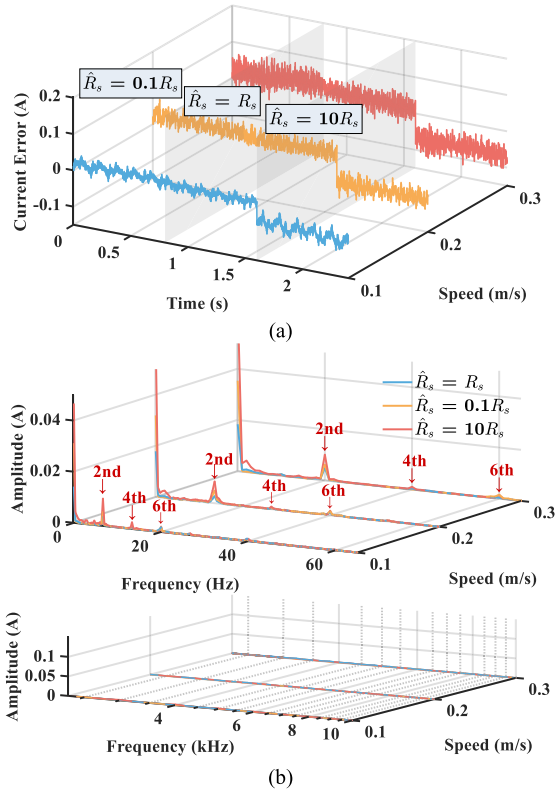

Fig. 9. Current errors and spectrum under resistance mismatches at three operating speeds. (a) Current errors. (b) The Spectrum.

Fig. 7. It is observed that there is noticeable asymmetry in the ac mutual inductance, which is consistent with FE results.

A. *Disturbance Validation Experiment*

In order to validate the impact of various disturbances, the experiments are conducted with different parameters. To clearly illustrate the frequency characteristics, the PMLSM operates at a constant speed. Since the detent force in PMLSM causes current ripples, the current tracking errors are presented to avoid the impact of these ripples. For the purpose of providing a more comprehensive illustration of the effects induced by various disturbances, experiments are conducted at speeds of 0.1 m/s, 0.2 m/s, and 0.3 m/s, with the corresponding experimental results plotted in three-dimensional figures for comparative analysis. At three operating speeds, the q-axis current tracking errors and their frequency spectra under different conditions of inductance, resistance, and flux linkage mismatches are depicted in Figs. 8–10, where $L_s = L_{d(q)}$. The frequency components of the current tracking errors in the low- and high-frequency domains are presented separately to enhance the clarity of each spectral region.

In Fig. 8, when the employed inductance is smaller than the real value, the dc and low-order harmonic components in tracking errors increase. However, when the employed inductance is greater than the real value, not only the low-frequency errors increase, but also the HF errors emerge. The frequency of HF errors is close to one-quarter of the sampling frequency.

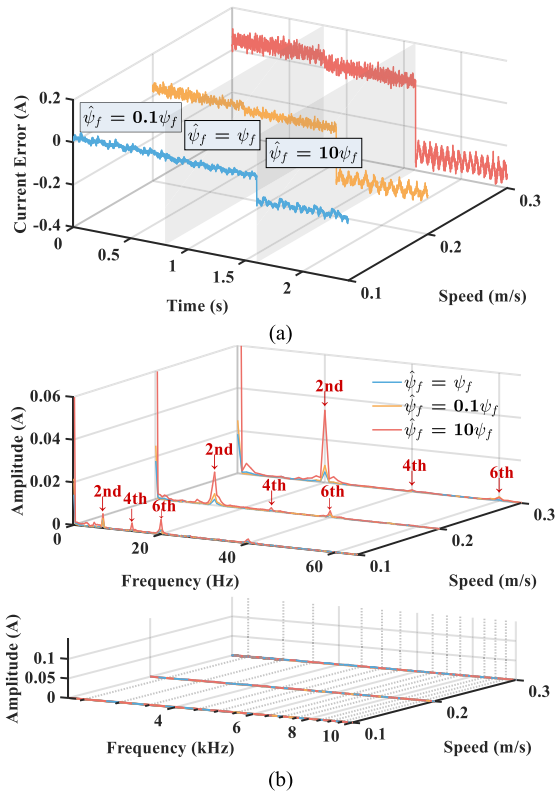

Fig. 10. Current errors and spectrum under flux linkage mismatches at three operating speeds. (a) Current errors. (b) The Spectrum.

It is evident that the frequencies of the disturbances caused by the excessive inductance are significantly higher than those of the remaining low-order harmonic components. In Figs. 9 and 10, the resistance and flux linkage mismatches lead to increased dc offset and low-order harmonic errors. Besides, it is observed that even with accurate parameters, there are still current tracking errors caused by unmodeled dynamics such as inverter nonlinearity. The HF components of these disturbances are negligible, with their spectral energy primarily concentrated in the low-order harmonic range. At different speeds, both the magnitude and frequency characteristics of the current tracking errors exhibit noticeable variations. As the speed increases, the associated resistive forces also rise, resulting in higher required reference currents. Consequently, the overall magnitude of the tracking errors increases accordingly. For the harmonic components in the current errors, speed variations lead to corresponding shifts in their frequencies. For HF errors caused by excessive inductance, parameter asymmetry introduces harmonics into their amplitude. As a result, the amplitude of the HF errors fluctuates more rapidly with increasing speed. However, since the fluctuation frequency remains significantly lower than the HF error frequency, the variation of speed has a negligible effect on the frequency of the HF errors. In summary, the various disturbances present in the asymmetric DPCC exhibit distinct spectral characteristics, encompassing both dc and harmonic components as well as HF components. Although the effects of various disturbances vary with operating speed, they consistently exhibit similar frequency distribution characteristics. Furthermore, the low- and high-frequency disturbances are well separated in the spectrum, which is consistent with theoretical analysis.

B. Robustness Performance Validation

To verify the robustness of the proposed DPCC against various disturbances, experiments are conducted with the proposed method under different parameter mismatch conditions. The bandwidth coefficient ω_{g} in the UDE is set to 200π, yielding a disturbance rejection bandwidth of 100 Hz. In the PMO, the finite time for observation is set to 0.1 s, and the convergence coefficient γ is chosen as 2×10^4 to ensure finite-time convergence. The LTI operator selects a delay operator with the delay time of 0.01 s. α is set to 0.5. Under no-load conditions with a speed of 0.1 m/s, the proposed robust method is initiated at 0.5 s. The experimental results with $\hat{R}_{\mathrm{s}} = R_{\mathrm{s}}/4$, $\hat{\psi}_{\mathrm{f}} = \psi_{\mathrm{f}}/4$, $\hat{L}_{\mathrm{d}} = L_{\mathrm{d}}/2$, $\hat{L}_{\mathrm{q}} = L_{\mathrm{q}}/2$ are shown in Fig. 11. Since there is no excessive inductance, the output of the PMO remains zero and is not presented. When the parameters are $\hat{R}_{\mathrm{s}} = 4R_{\mathrm{s}}$, $\hat{\psi}_{\mathrm{f}} = 4\psi_{\mathrm{f}}$, $\hat{L}_{\mathrm{d}} = 2L_{\mathrm{d}}$, $\hat{L}_{\mathrm{q}} = 2L_{\mathrm{q}}$, the results are shown in Fig. 12. In this case, to verify the tracking capability for time-varying mismatches, the asymmetry parameters are set to zero, i.e., $\gamma = 0$, $b_{\mathrm{r}} = 0$.

In Fig. 11, since no factors induce HF disturbances, UDE can suppress all disturbances. Due to the rapid convergence of UDE, it can effectively mitigate the dc and second harmonic tracking errors within a time much shorter than T_{f}. In Fig. 12, within the finite time T_{f} after the proposed method is initiated, the PMO is activated for observation. The UDE alone is insufficient for

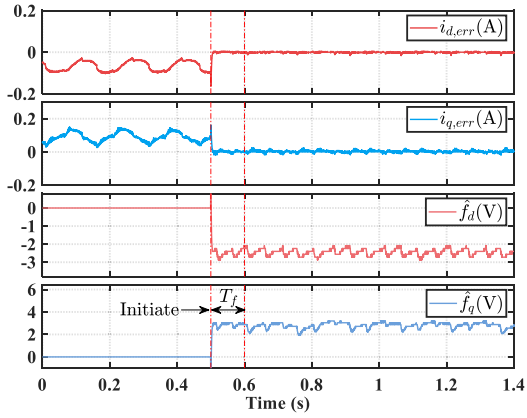

Fig. 11. Tracking results with $\hat{R}_{\mathrm{s}} = R_{\mathrm{s}}/4$, $\hat{\psi}_{\mathrm{f}} = \psi_{\mathrm{f}}/4$, $\hat{L}_{\mathrm{d}} = L_{\mathrm{d}}/2$, $\hat{L}_{\mathrm{q}} = L_{\mathrm{q}}/2$.

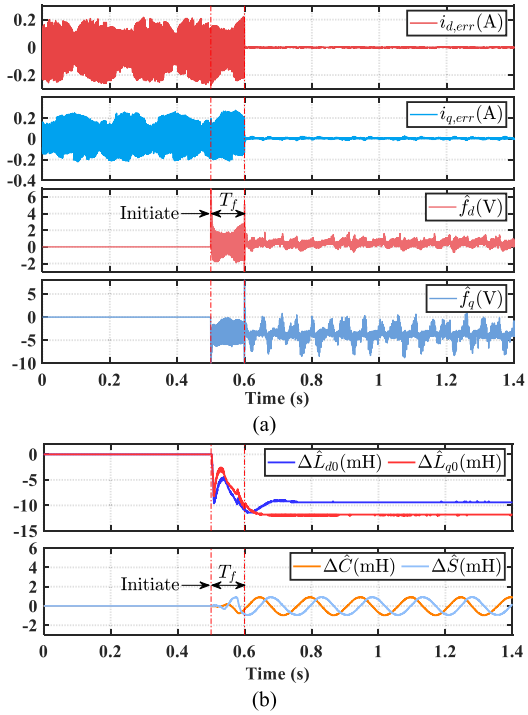

Fig. 12. Tracking results with $\hat{R}_{\mathrm{s}} = 4R_{\mathrm{s}}$, $\hat{\psi}_{\mathrm{f}} = 4\psi_{\mathrm{f}}$, $\hat{L}_{\mathrm{d}} = 2L_{\mathrm{d}}$, $\hat{L}_{\mathrm{q}} = 2L_{\mathrm{q}}$. (a) Tracking errors and estimated disturbances. (b) Observed mismatches.

complete suppression of HF disturbances. Upon reaching T_{f}, the observed mismatches are employed for compensation. At this point, all disturbances across the spectrum are eliminated, thereby significantly reducing the tracking errors. During observation, the DSOGI tracks the second-harmonic asymmetric components, which involves a relatively long transient process. On the other hand, the original output from the finite-time observer converges rapidly, which can impact the dynamic process of the DSOGI. Nevertheless, since the original observation can converge within the finite time, fluctuations during the transient process do not affect the results. Moreover, the impact of fluctuations on the control results is minimal according to the experimental results. The mismatch value obtained from the PMO are $\Delta\hat{\mathrm{L}}_{\mathrm{d0}} = -9.6$ mH, $\Delta\hat{\mathrm{L}}_{\mathrm{q0}} = -11.4$ mH, $\Delta\hat{\gamma} = 1.04$ mH, $\Delta\hat{\mathrm{b}}_{\mathrm{r}} = 110^\circ$. The observation errors for the *d*- and

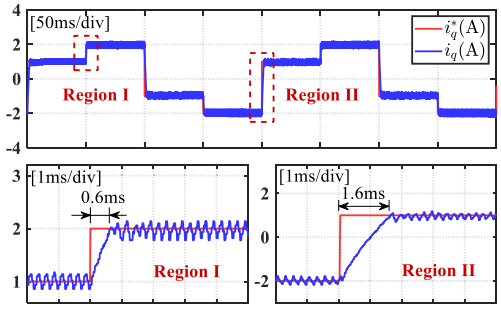

Fig. 13. Current step response results with the conventional DPCC.

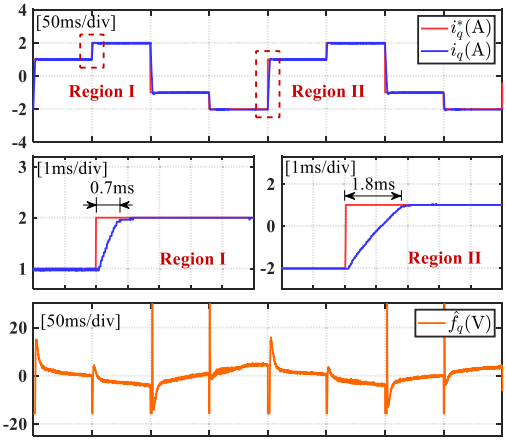

Fig. 14. Current step response results with the proposed robust DPCC.

q-axis symmetric inductance mismatches are both within 5%, while the errors for the asymmetric magnitude and phase are -7.6% and 8.3% . The level of accuracy ensures that disturbances can be effectively suppressed even with significant initial parameter mismatches. The above experimental results validate that the proposed method is capable of accurately observing and compensating for disturbances arising from various parameter mismatches, thereby effectively enhancing the robustness of the asymmetric DPCC.

C. Dynamic Performance Validation

To verify the dynamic performance of the proposed method, step response experiments for current and speed are conducted. In the experiments, the parameters are set as $\hat{R}_\mathrm{s} = 4R_\mathrm{s}$, $\hat{\psi}_\mathrm{f} = 4\psi_\mathrm{f}$, $\hat{L}_\mathrm{d} = 2L_\mathrm{d}$, $\hat{L}_\mathrm{q} = 2L_\mathrm{q}$.

In the current step experiment, the reference trajectory is a piecewise step function with values of ±1 A and ±2 A. The current tracking results of the conventional DPCC and the proposed robust DPCC are shown in Figs. 13 and 14.

In Fig. 13, the significant tracking errors occur with conventional DPCC. In the zoomed-in region, it is observed that the real current exhibits HF oscillations around the reference current. In Fig. 14, the observed lumped disturbance varies in accordance with the reference current. Comparing with Fig. 13, compensating for the disturbances resulting in a significant reduction in the tracking errors. In Regions I and II, the time required for the current to track the step trajectory shows a slight increase, which is

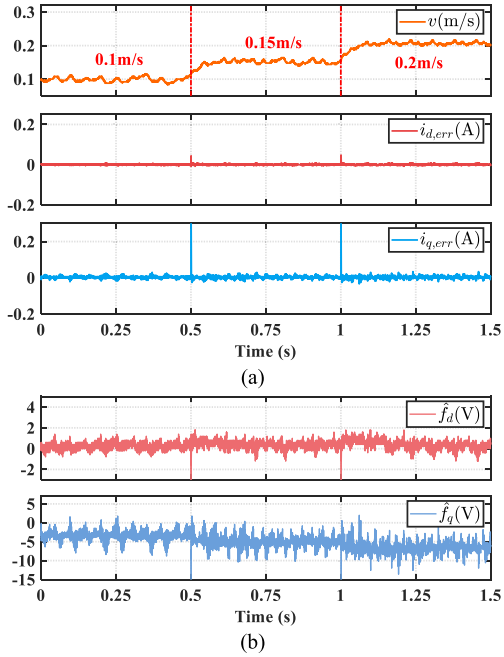

Fig. 15. Speed step response results with the proposed robust DPCC. (a) Speed and current tracking errors. (b) Estimated disturbances.

an expected outcome following the correction of the proportional coefficient in DPCC. More importantly, the real current can track the reference current without producing additional overshoot. Therefore, in the presence of abrupt variations in the current trajectory, the proposed method can enhance robustness of the current tracking without compromising dynamic performance.

In the speed step experiment, the reference speeds are set to 0.1, 0.15 and 0.2 m/s, respectively. The experimental results with the proposed method are shown in Fig. 15.

In Fig. 15, the fluctuations of speed are attributed to the inherent detent force present within the PMLSM. Under different speed conditions, the frequency of the observed disturbances vary, and the current tracking errors are effectively suppressed. During the speed step changes, transient processes arise in the observed disturbances, and there are sudden increases in current tracking errors. However, the errors can recover quickly, thereby maintaining excellent tracking performance. Overall, the current and speed step response experiments demonstrate that the proposed method exhibits notable robustness against external disturbances, while maintaining rapid and stable dynamic performance.

D. Comparison Validation Experiment

To validate the advantages of the proposed robust DPCC, comparative experiments are conducted with existing disturbance rejection methods. According to [8], the ESO can effectively observe model dynamics and lumped disturbance, making it suitable for comparison. In addition, the comparative experiments also include the enhanced DPCC with LDO proposed in [26]. In this method, the disturbance rejection capability of the LDO is enhanced, and additional inductance and inverter disturbance observer is proposed to broaden the scope

of disturbance observation. Due to its similarity in disturbance rejection framework to the proposed method, the comparison results can further highlight the characteristics and advantages of the proposed method. This method involves a combination of observed disturbances similar to the lumped disturbances addressed in both ESO and the proposed method. Thus, these observed disturbances are extracted and combined as the lumped disturbances to facilitate the comparison. In the experiments, all methods are activated at the beginning, with the parameters set to $\hat{R}_{\rm s} = 4R_{\rm s}$, $\hat{\psi}_{\rm f} = 4\psi_{\rm f}$, $\hat{L}_{\rm d} = 2L_{\rm d}$, $\hat{L}_{\rm q} = 2L_{\rm q}$. To enable a more comprehensive comparison, experiments are conducted at speeds of 0.1 m/s and 0.3 m/s. The current tracking errors and the observed lumped disturbances for the three methods under two speed conditions are shown in Figs. 16 and 17.

In Fig. 16, the observed lumped disturbances in the ESO and the proposed method contain multiple frequency components. In comparison, the observed disturbances in the enhanced DPCC exhibit low-frequency characteristics due to the absence of HF disturbance modeling. However, the observed inductance values utilized for HF disturbance rejection are inherently included within the presented disturbances. As shown in Fig. 16(a), due to the limited disturbance rejection bandwidth of the ESO, it can only compensate for low-frequency disturbances and cannot eliminate the effects of HF disturbances. As a result, the current tracking errors remain pronounced after the ESO compensation. In the experimental results of the enhanced DPCC shown in Fig. 16(b), the tracking errors significantly decrease with the update of the inductance observer. However, since this method is unable to effectively observe the time-varying and coupled inductances, it cannot eliminate all disturbances in the asymmetric model. Consequently, current tracking errors arising from asymmetry still persist. According to Fig. 16(c), the proposed method accounts for the time-varying and coupling characteristics induced by asymmetry in both parameter mismatch observation and disturbance rejection. Therefore, it is capable of mitigating the impact of various disturbances, thereby achieving the most stable and reliable current tracking performance. Fig. 17 shows that higher speed leads to longer dynamic response times. Moreover, all three methods can effectively observe and suppress the disturbances arising during the dynamic process. Compared to the results at 0.1 m/s, the frequencies of the current tracking errors and observed disturbances increase at a higher speed. As demonstrated in Fig. 17, at the speed of 0.3 m/s, the disturbance rejection bandwidth of all three methods is sufficient to ensure stable attenuation of both dc offsets and harmonic disturbances. For HF disturbances, the ESO still fails to achieve effective observation. In Fig. 17(b), the convergence rate of the inductance observer in the enhanced DPCC is increased, and its updates lead to a significant reduction in the tracking errors. However, it still cannot accurately estimate the asymmetric time-varying inductance whose frequency also increases with speed, resulting in residual tracking errors. The results in Fig. 17(c) confirm that the proposed method maintains reliable observation of time-varying mismatches and disturbances at a higher speed, ensuring effective disturbance rejection. Therefore, the proposed method demonstrates robustness to variations of speed.

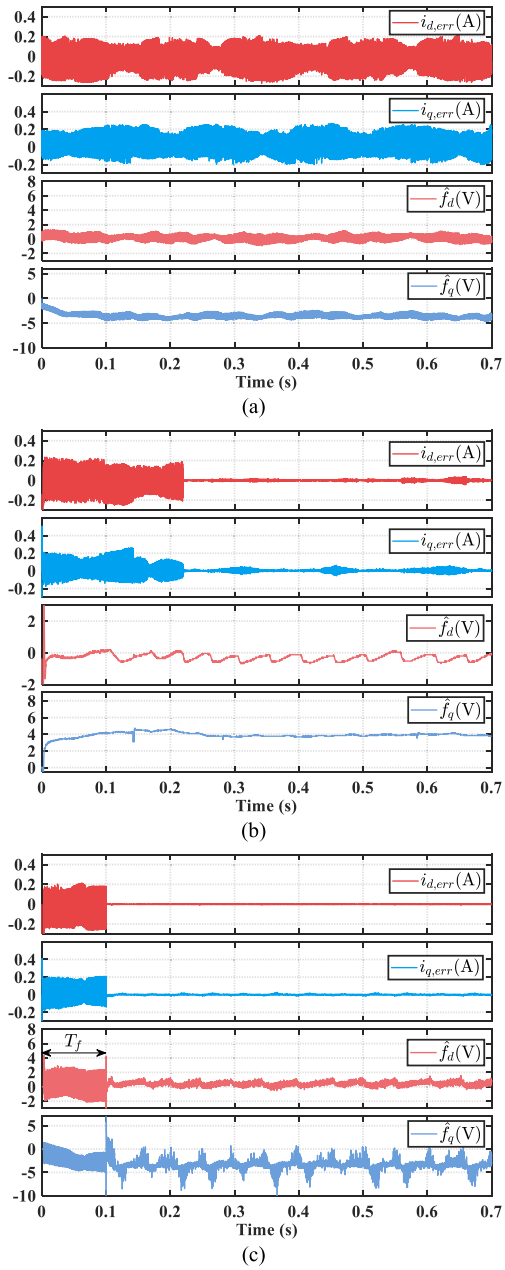

Fig. 16. Experimental results at 0.1m/s with $\hat{R}_{\rm s} = 4R_{\rm s}$, $\hat{\psi}_{\rm f} = 4\psi_{\rm f}$, $\hat{L}_{\rm d} = 2L_{\rm d}$, $\hat{L}_{\rm q} = 2L_{\rm q}$. (a) ESO method. (b) Enhanced DPCC. (c) Proposed method.

To further demonstrate the adaptability and stability of the proposed method in addressing time-varying and coupled inductances, additional inductance disturbances are injected in the experiments. After disturbance injection, the frequency of the time-varying inductance is set to 20 Hz. In the DPCC implementation, the variation range of the employed $\hat{L}_{\rm d(q)}$ is $[0.5L_{\rm d(q)}, 2L_{\rm d(q)}]$, and the amplitude of the injected coupled inductance $\hat{L}_{\rm dq}$ is set to 3 mH. To eliminate the influence of resistance and flux linkage on the experimental comparison, their initial values are both set to zero. The comparative experiments between the enhanced DPCC and the proposed method are conducted at speeds of 0.1 m/s and 0.3 m/s. In both methods, the compensation mechanisms are activated at 0.1 s. Figs. 18 and 19 present the

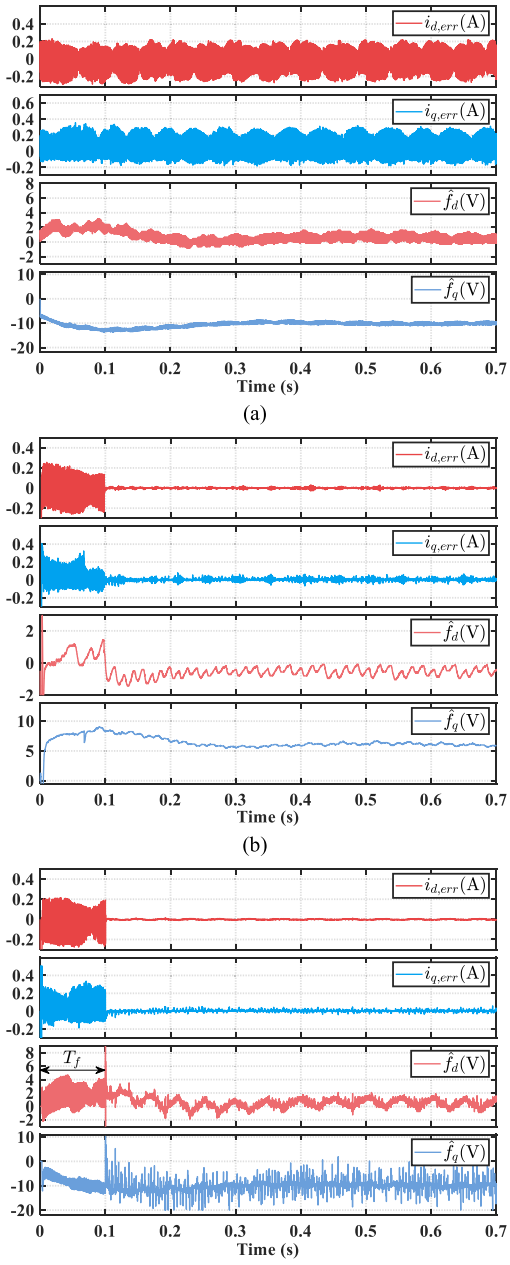

Fig. 17. Experimental results at 0.3 m/s with $\hat{R}_s = 4R_s$, $\hat{\psi}_f = 4\psi_f$, $\hat{L}_d = 2L_d$, $\hat{L}_q = 2L_q$. (a) ESO method. (b) Enhanced DPCC. (c) Proposed method.

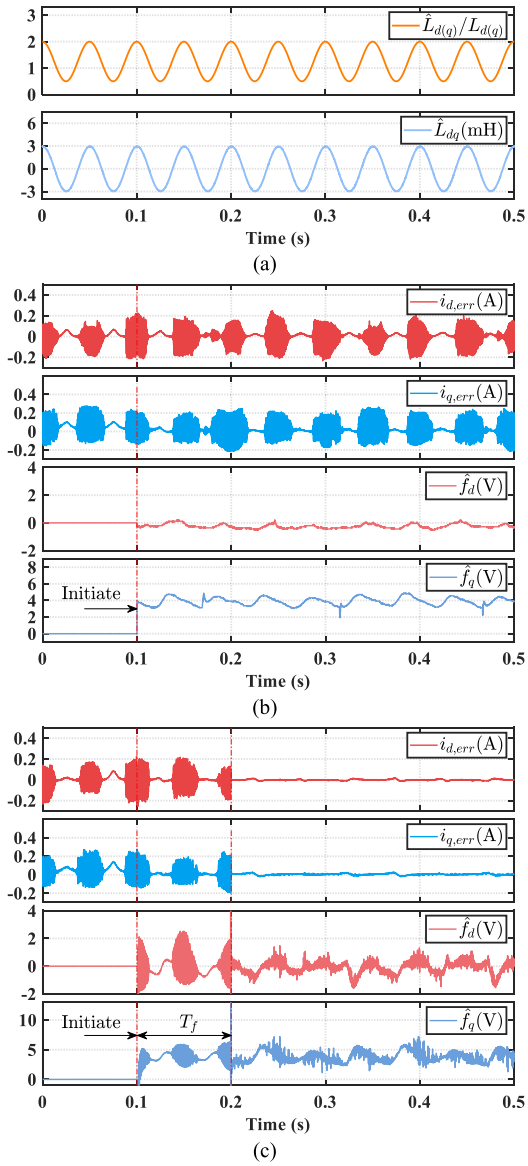

Fig. 18. Comparison experimental results with injected inductance disturbances at 0.1 m/s. (a) Time-varying and coupled inductances. (b) Enhanced DPCC with LDO. (c) Proposed method.

time-varying and coupled inductance, current tracking errors, and observed lumped disturbances of the two methods at both speeds.

In Fig. 18, in the absence of compensation, the time-varying and coupled inductance parameters give rise to significant current tracking errors. Moreover, the frequencies of these errors vary from low to high as the inductance parameters change. The experimental results in Fig. 18(b) indicate that the enhanced DPCC with LDO cannot continuously and accurately observe the inductance with rapid and large-range variations. Moreover, its inability in effectively observing the coupled inductance poses a significant challenge in mitigating the influence of coupling-induced disturbances on the observation and control. Therefore, this method fails to exhibit satisfactory compensation and suppression performance with respect to time-varying and coupled inductance disturbances. As illustrate in Fig. 18(c), following the completion of observation and compensation by the PMO within the finite time, the effects of time-varying and coupled inductance disturbances are significantly suppressed, thereby effectively mitigating the current tracking errors. In Fig. 19, since the injected inductance disturbances remain unchanged at 0.3 m/s, the tracking errors exhibit minimal variation. The magnitude of the observed disturbances increases for both methods as the speed rises. In Fig. 19(b), the inductance observer in the enhanced DPCC updates more frequently at a higher speed. Besides, the shorter duration of each update interval leads to reduced fluctuations in the observer output. However, due to the lack of an observation mechanism specifically designed

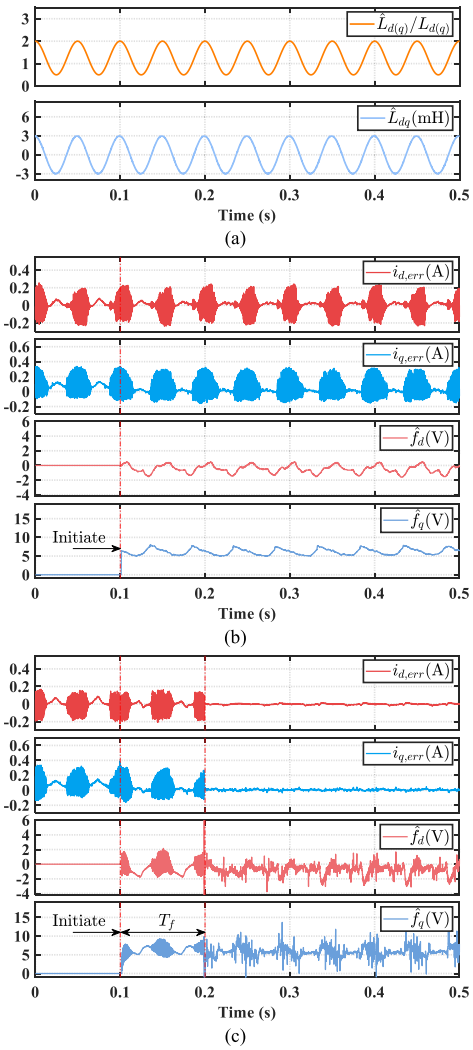

Fig. 19. Comparison experimental results with injected inductance disturbances at 0.3 m/s. (a) Time-varying and coupled inductances. (b) Enhanced DPCC with LDO. (c) Proposed method.

for rapidly time-varying and coupled inductance, the enhanced DPCC still fails to achieve effective disturbance rejection. As depicted in Fig. 19(c), the proposed method retains its ability to reliably observe the injected inductance disturbances, thereby maintaining stable current tracking performance at 0.3 m/s. The aforementioned results underscore the enhanced robustness and stability of the proposed method in addressing time-varying and coupled inductance disturbances compared to other disturbance suppression methods. Furthermore, the adaptability of the proposed method under different speed conditions has also been validated.

VI. Conclusion

A robust DPCC of PMLSMs based on the time-varying asymmetric model is proposed. The UDE is integrated into the deadbeat control framework to suppress the lumped disturbances. The PMO is introduced to observe inductance mismatches, thereby extending the disturbance rejection bandwidth. The proposed robust DPCC outperforms conventional methods in addressing the time-varying and coupling characteristics of the asymmetric model. The advantages of the proposed method have been validated through experiments, which can be concluded as follows.

1) It has enhanced adaptability. It is applicable for time-varying systems arising from asymmetric DPCC and can provide rigorous stability proofs. Model disturbances, unmodeled dynamics and external disturbances in the asymmetric DPCC can be significantly suppressed by the proposed method. Compared to conventional methods, it offers broader applicability and improved adaptability in disturbance rejection.
2) It exhibits excellent steady-state and dynamic performance. The observation errors of the mismatched symmetric inductance remain within 5%, while the error of the asymmetric magnitude is -7.6%, and thus ensuring compensation accuracy. Besides, during working condition changes, the transient response of the current tracking converges quickly with minimal overshoot.
3) It demonstrates superior robustness. It effectively addresses the challenges posed by time-varying and HF disturbances in the asymmetric model, thereby improving the disturbance suppression capability. Even under rapid and large-range parameter variations, the proposed method achieves precise and stable current tracking.

References

[1] K. Zhang, L. Wang, and X. Fang, "Adaptive nonlinear speed tracking control of permanent magnet linear synchronous motor based on I&I theory," *IEEE Trans. Ind. Appl.*, vol. 60, no. 5, pp. 7835–7843, Sep./Oct. 2024.
[2] D. Fu, X. Zhao, and J. Zhu, "A novel robust super-twisting nonsingular terminal sliding mode controller for permanent magnet linear synchronous motors," *IEEE Trans. Power Electron.*, vol. 37, no. 3, pp. 2936–2945, Mar. 2022.
[3] A. D. Alexandrou, N. K. Adamopoulos, and A. G. Kladas, "Development of a constant switching frequency deadbeat predictive control technique for field-oriented synchronous permanent-magnet motor drive," *IEEE Trans. Ind. Electron.*, vol. 63, no. 8, pp. 5167–5175, Aug. 2016.
[4] Q. Xu and S. Fang, "Robust deadbeat predictive current sensorless control for permanent magnet synchronous motor," *IEEE Trans. Power Electron.*, vol. 39, no. 9, pp. 11441–11454, Sep. 2024.
[5] C. Xu, Z. Han, and S. Lu, "Deadbeat predictive current control for permanent magnet synchronous machines with closed-form error compensation," *IEEE Trans. Power Electron.*, vol. 35, no. 5, pp. 5018–5030, May 2020.
[6] Y. Yao, Y. Huang, F. Peng, J. Dong, and H. Zhang, "An improved deadbeat predictive current control with online parameter identification for surface-mounted PMSMs," *IEEE Trans. Ind. Electron.*, vol. 67, no. 12, pp. 10145–10155, Dec. 2020.
[7] X. Sun, S. Zhang, Z. Yang, G. Lei, and T. Li, "Improved DPCC and parameter identification for permanent magnet synchronous motors with current error compensation," *IEEE Trans. Ind. Electron.*, to be published, doi: 10.1109/TIE.2025.3553157.
[8] J. Yang, W.-H. Chen, S. Li, L. Guo, and Y. Yan, "Disturbance/uncertainty estimation and attenuation techniques in PMSM drives—A survey," *IEEE Trans. Ind. Electron.*, vol. 64, no. 4, pp. 3273–3285, Apr. 2017.
[9] L. He, J.W. F. Wang, and J. Rodríguez, "Zynq implemented Luenberger disturbance observer based predictive control scheme for PMSM drives," *IEEE Trans. Power Electron.*, vol. 35, no. 2, pp. 1770–1778, Feb. 2020.
[10] X. Sun, J. Cao, G. Lei, Y. Guo, and J. Zhu, "A robust deadbeat predictive controller with delay compensation based on composite sliding-mode observer for PMSMs," *IEEE Trans. Power Electron.*, vol. 36, no. 9, pp. 10742–10752, Sep. 2021.

[11] X. Sun, X. Lin, D. Guo, G. Lei, and M. Yao, "Improved deadbeat predictive current control with extended state observer for dual three-phase PMSMs," *IEEE Trans. Power Electron.*, vol. 39, no. 6, pp. 6769–6782, Jun. 2024.
[12] B. H. B. Boff, P. R. Eckert, and Y. Amara, "A comprehensive review on the end effects of linear permanent magnet machines," *IEEE Trans. Ind. Appl.*, vol. 59, no. 2, pp. 1728–1741, Mar./Apr. 2023.
[13] X. Huang, J. Liang, Z. Qian, and J. Li, "An iterative estimation algorithm of prepositioning focusing on the detent force in the permanent magnet linear synchronous motor system," *IEEE Trans. Ind. Electron.*, vol. 67, no. 10, pp. 8252–8261, Oct. 2020.
[14] M. Zheng, Z. Zou, Q. Lu, Y. Li, and Y. Shen, "A simple modified deadbeat direct thrust control for permanent magnet linear synchronous machine considering parameter asymmetry," *IEEE Trans. Ind. Appl.*, vol. 59, no. 3, pp. 3163–3174, May/Jun. 2023.
[15] Z. Zou, M. Zheng, Y. Li, Q. Lu, and J. Cui, "Robustness analysis and enhancement of deadbeat predictive control for permanent magnet linear synchronous machines with asymmetric model," in *Proc. 26th Int. Conf. Elect. Machines Syst.*, 2023, pp. 755–760.
[16] S. Dai, J. Wang, Z. Sun, and E. Chong, "Multiple current harmonics suppression for low-inductance PMSM drives with deadbeat predictive current control," *IEEE Trans. Ind. Electron.*, vol. 69, no. 10, pp. 9817–9826, Oct. 2022.
[17] W. Wang, C. Liu, Z. Song, and Z. Dong, "Harmonic current suppression for dual three-phase PMSM based on deadbeat control and disturbance observer," *IEEE Trans. Ind. Electron.*, vol. 70, no. 4, pp. 3482–3492, Apr. 2023.
[18] F. Yang, X. Zhao, H. Jin, X. Wang, and X. Liu, "Improved deadbeat predictive current control with embedded resonant polynomial and disturbance observer for pmsm current distortion rejection," *IEEE J. Emerg. Sel. Topics Power Electron.*, vol. 12, no. 2, pp. 1934–1945, Apr. 2024.
[19] R. Yang, M. Wang, L. Li, G. Wang, and C. Zhong, "Robust predictive current control of PMLSM with extended state modeling based kalman filter: For time-varying disturbance rejection," *IEEE Trans. Power Electron.*, vol. 35, no. 2, pp. 2208–2221, Feb. 2022.
[20] F. Amato, *Robust Control of Linear Systems Subject to Uncertain Time-Varying Parameters*, Berlin, Germany: Springer, 2006.
[21] Q.-C. Zhong, A. Kuperman, and R. K. Stobart, "Design of UDE-based controllers from their two-degree-of-freedom nature," *Int. J. Robust Nonlinear Control*, vol. 21, no. 17, pp. 1994–2008, Nov. 2011.
[22] J. Ren, Y. Ye, G. Xu, Q. Zhao, and M. Zhu, "Uncertainty-and-disturbance-estimator-based current control scheme for PMSM drives with a simple parameter tuning algorithm," *IEEE Trans. Power Electron.*, vol. 32, no. 7, pp. 5712–5722, Jul. 2017.
[23] Y. Xiong, Y. Ye, and M. Zhu, "UDE-based current controller with enhanced grid frequency fluctuation adaptability for LCL-type grid-tied inverters," *IEEE Trans. Power Electron.*, vol. 38, no. 2, pp. 1683–1691, Feb. 2023.
[24] H. Wang, C. Gan, C. Zhang, H. Ren, and R. Qu, "Parameter robust predictive current control for PMSM drives based on self-tuning incremental model and voltage constraint compensation," *IEEE Trans. Power Electron.*, vol. 40, no. 8, pp. 11268–11282, Aug. 2025.
[25] X. Huang, Q. Hu, Z. Liu, W. Li, G. Yang, and Z. Li, "A robust deadbeat predictive current control method for IPMSM," *IEEE Trans. Transp. Electrific.*, vol. 10, no. 3, pp. 4722–4733, Sep. 2024.
[26] X. Yuan, S. Xie, J. Chen, S. Zhang, C. Zhang, and C. H. T. Lee, "An enhanced deadbeat predictive current control of SPMSM with linear disturbance observer," *IEEE J. Emerg. Sel. Topics Power Electron.*, vol. 10, no. 5, pp. 6304–6316, Oct. 2022.
[27] Z. Zou, M. Zheng, Y. Li, Q. Lu, and Z. Q. Zhu, "Full electrical parameter estimation method of PMLSM considering parameter asymmetry without external excitation," *IEEE Trans. Power Electron.*, vol. 39, no. 10, pp. 12937–12950, Oct. 2024.
[28] Z. Zou, M. Zheng, Y. Li, and Q. Lu, "A novel full electrical parameters estimation method of permanent magnet linear synchronous machines considering parameter asymmetry," *IEEE Trans. Ind. Electron.*, vol. 71, no. 9, pp. 10256–10267, Sep. 2024.
[29] H. Ríos, D. Efimov, J. A. Moreno, W. Perruquetti, and J. G. Rueda-Escobedo, "Time-varying parameter identification algorithms: Finite and fixed-time convergence," *IEEE Trans. Autom. Control*, vol. 62, no. 7, pp. 3671–3678, Jul. 2017.
[30] S. Aranovskiy, A. Bobtsov, R. Ortega, and A. Pyrkin, "Performance enhancement of parameter estimators via dynamic regressor extension and mixing," *IEEE Trans. Autom. Control*, vol. 62, no. 7, pp. 3546–3550, Jul. 2017.
[31] K. S. Narendra and A. M. Annaswamy, "Persistent excitation in adaptive systems," *Int. J. Control*, vol. 45, no. 1, pp. 127–160, 1987.

Ziyu Zou (Graduate Student Member, IEEE) was born in Zhejiang, China, in 1999. He received the B.Eng. degree in electrical engineering in 2021 from Zhejiang University, Hangzhou, China, where he is currently working toward the Ph.D. degree in electrical engineering.

His research interests include the motor drive and control of permanent magnet linear machines.

Mengfei Zheng was born in Fuzhou, China, in 1994. He received the B.Eng. and M.Sc. degrees from Fuzhou University, Fuzhou, China, in 2016 and 2019, respectively, and the Ph.D. degree from the College of Electrical Engineering, Zhejiang University, Hangzhou, China, all in electrical engineering.

His research interests include analysis and control of permanent magnet linear machines, planar machines.

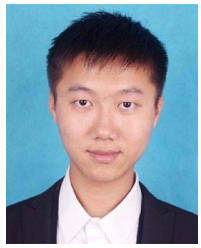

Yanxin Li (Member, IEEE) received the B.Eng. and M.Eng. degrees from Zhejiang University, Hangzhou, China, in 2011 and 2014, respectively, and the Ph.D. degree from the University of Sheffield, Sheffield, U.K., in 2018, all in electrical engineering.

Since 2020, he has been a tenure-tracked Associate Professor with the Zhejiang University. His major research interests include the modeling, design, and analysis of linear machines.

Qinfen Lu (Senior Member, IEEE) received the B.Eng., M.Sc., and Ph.D. degrees in electrical engineering from Zhejiang University, Hangzhou, China, in 1996, 1999, and 2005, respectively.

Since 1999, she has been with the College of Electrical Engineering, Zhejiang University, where she is currently a Professor. Since 2019, she has also been a part-time Professor with the Lanzhou University of Technology, Lanzhou, China. Her research interests include analysis and control of linear machines and permanent magnet machines.